Wolfgang Müller · Simon P. Kelley · Igor M. Villa

Dating fault-generated pseudotachylytes: comparison of ^{40}Ar/^{39}Ar stepwise-heating, laser-ablation and Rb–Sr microsampling analyses

Abstract Three different geochronological techniques (stepwise-heating, laser-ablation ^{40}Ar/^{39}Ar, Rb–Sr microsampling) have been evaluated for dating fault-generated pseudotachylytes sampled along the Periadriatic Fault System (PAF) of the Alps. Because pseudotachylytes are whole-rock systems composed of melt, clast and alteration phases, chemical control from both Ar isotopes (Cl/K, Ca/K ratios) and EMPA analyses is crucial for their discrimination. When applied to stepwise-heating ^{40}Ar/^{39}Ar analyses, this approach yields accurate melt-related ages, even for complex age spectra. The spatial resolution of laser-ablation ^{40}Ar/^{39}Ar analyses is capable of contrasting melt, clast and alteration phases in situ, provided the clasts are not too fine grained, the latter of which results in integrated "mixed" ages without geological information. Elevated Cl/K and Ca/K ratios were found to be an invaluable indicator for the presence of clast admixture or inherited ^{40}Ar. Due to incomplete isotopic resetting during frictional melting, Rb–Sr microsampling dating did not furnish geologically meaningful ages. On the basis of isotopic disequilibria among pseudotachylyte matrix phases, and independent Rb–Sr microsampling dating of cogenetic (ultra)mylonites, the concordant ^{40}Ar/^{39}Ar pseudotachylyte ages are interpreted as formation ages. The investigated pseudotachylytes altogether reveal a Cretaceous to Miocene history for the entire PAF, consistent with independent geological evidence. Individual faults, however, consistently reveal narrower intervals of enhanced activity lasting a few million years. Electronic supplementary material to this paper can be obtained by using the Springer LINK server at http://dx.doi.org/10.1007/s00410-002-0381-6

W. Müller (✉)
Department Erdwissenschaften, ETH Zürich,
8092 Zürich, Switzerland
E-mail: wolfgang.mueller@anu.edu.au
Tel.: +61-2-61259968
Fax: +61-2-62572737

S.P. Kelley
Department of Earth Sciences,
The Open University, Milton Keynes, MK7 6AA, UK

I.M. Villa
Gruppe Isotopengeologie, Universität Bern,
3012 Bern, Switzerland

Present address: W. Müller
Research School of Earth Sciences,
The Australian National University,
Canberra, ACT 0200, Australia

Editorial responsibility: J. Hoefs

Introduction

Pseudotachylytes are common rocks in upper crustal fault zones. They are interpreted to represent products of frictional melting, generated mostly during (co-)seismic faulting at the brittle ductile transition (for a review see Magloughlin and Spray 1992; Sibson 1975; Spray 1995). Additionally, pseudotachylytes can be generated as shock melts during meteorite impacts (Martini 1991; White 1993) and (rarely) under eclogite facies conditions (Austrheim and Boundy 1994).

In contrast to other fault rocks within (semi-)brittle fault zones such as cataclasites or fault gouges, pseudotachylytes are generated during short-lived, high-temperature processes. As outlined by Spray (1992), pseudotachylyte formation can be considered in terms of the melting and comminution properties of the minerals constituting the pseudotachylyte host rock. When considering the K–Ar system, the major K-bearing minerals micas, amphiboles and, to a lesser extent, also K-feldspar and low-Ca plagioclase are characterised by relatively low melting points, low values for their respective hardness and yield strengths, and also low thermal conductivities (cf. Fig. 5 in Spray 1992). These K-bear-

ing minerals are most easily comminuted by both abrasion and thermal shock and will form fine-grained aggregates which are most susceptible to frictional melting, given their low melting points and high water contents. Petrographic observations of surviving clasts within the pseudotachylyte matrix support this model, since clasts are never composed of micas or amphiboles but mostly of quartz and high-Ca plagioclase, both characterised by high melting points.

Because of this peculiar formation mechanism, it can be expected that phases newly crystallised from a degassed melt may incorporate no initial Ar and therefore give correct K–Ar ($^{40}Ar/^{39}Ar$) ages. However, given the short time involved during frictional melting (Sibson 1975; Kelley et al. 1994), Ar may only incompletely escape from the pseudotachylyte melt, resulting in the presence of inherited ^{40}Ar which additionally complicates the dating of pseudotachylytes.

For the Rb–Sr system, the Sr isotopic resetting behaviour following frictional melting appears to be less favourable (e.g. Hammouda et al. 1996). Plagioclase, the major reservoir for Sr, is not always completely resorbed by the melt and complete Rb–Sr isotopic (re)homogenisation by frictional melting cannot be expected. Diffusion of Sr in plagioclase is slow at the temperatures of frictional melting (Gilletti and Casserly 1994) and no equilibrium will be reached during a short-lived melting event.

It follows that dating of pseudotachylytes is feasible mainly utilising the $^{40}Ar/^{39}Ar$ technique(s), although some apparently successful applications of Rb–Sr dating to pseudotachylytes have been reported (Reimold and Oskierski 1987; Thöni 1988; Petermann and Day 1989). By contrast, other types of brittle fault rocks such as cataclasites and fault gouges pose great difficulties for dating (e.g. van der Pluijm et al. 2001). An increasing number of publications on dating both impact and fault-related pseudotachylytes has been published recently. The methods applied include stepwise-heating $^{40}Ar/^{39}Ar$ (Reimold et al. 1990, 1992; Trieloff et al. 1994), laser-ablation $^{40}Ar/^{39}Ar$ (Kelley et al. 1994; Spray et al. 1995; Kelley and Spray 1997; Magloughlin et al. 2001; Sherlock and Hetzel 2001), K–Ar (Andriessen et al. 1979; Thöni 1981), Rb–Sr (Reimold and Oskierski 1987; Thöni 1988; Petermann and Day 1989) and fission track on the glassy matrix (Seward and Sibson 1985).

This paper aims to compare and evaluate the potential of stepwise-heating and laser-ablation $^{40}Ar/^{39}Ar$ and Rb–Sr microsampling analyses for dating pseudotachylyte samples with different compositions and tectonic origin. Particular emphasis is given to the combination of $^{40}Ar/^{39}Ar$ chronological information and pseudotachylyte chemistry derived from both Ar isotopes and EMPA analyses. This approach is fundamental for a discrimination between melt, clast and alteration phases and a successful interpretation of pseudotachylyte ages.

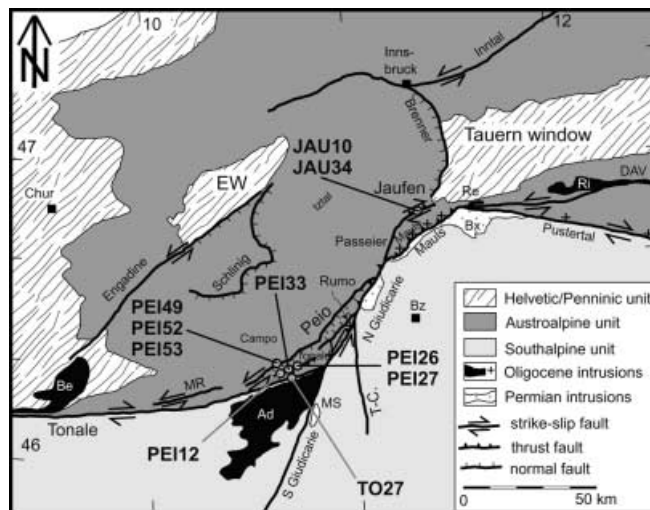The pseudotachylytes investigated were collected along various faults related to the Periadriatic (Insubric)

Fig. 1. Simplified tectonic sketch map of the Alps showing the Periadriatic fault system and related major faults (based on Bigi et al. 1990, modified after Spiess 1995; Glutz 1997; Parolini 1997; Froitzheim et al. 1997; Fügenschuh et al. 2000). Sample locations are marked. Fault (segments): *MR* Mortirolo, *T-C* Trento-Cles, *DAV* Defereggen-Anterselva/Antholz-Valles/Vals. Plutons: *Be* Bregaglia/Bergell, *Ad* Adamello-Presanella, *MS* Monte Sabion, *Bx* Bressanone/Brixen, *Re* Rensen, *Ri* Vedrette di Ries/Rieserferner. *EW* Engadine window

Fault System (PAF) of the Alps (Fig. 1). Independent control on the pseudotachylyte ages presented here is provided by Rb–Sr microsampling ages of (ultra)mylonites from the same fault zones.

Experimental methods

Stepwise heating $^{40}Ar/^{39}Ar$

After initial sample selection by petrographic microscopy, 1.2-mm cores were drilled out of optically clast-free matrix areas from interior parts of the veins in ~1-cm-thick rock slices using a diamond core drill. Drills with diameters < 1 mm did not permit the recovery of cores. The cores were ultrasonically cleaned in acetone, alcohol and deionised water and checked for clasts, cracks and other inhomogeneities under a binocular microscope. As far as possible, only cores free of visible heterogeneities were weighed (~10–100 mg), wrapped in aluminium foil and irradiated at the TRIGA reactor in Pavia (Italy), except for sample PEI12 which was irradiated at the Risø reactor (Denmark). Variations of neutron fluxes along the length of the irradiation assembly were monitored using the interlaboratory standards FCT (27.95 Ma; Renne et al. 1994) and (rarely) MMhb-1 (520.4 Ma; Samson and Alexander 1987). Although Renne et al. (1998) provided updated values for the ages of those neutron flux monitors (~0.2–0.5% higher), we utilise the older calibration in order to maintain integrity with Müller (1998) and Müller et al. (2001). Using the newer calibration would not change any conclusion drawn in this paper. Samples were incrementally heated in a double-vacuum resistance furnace using identical heating schedules as far as possible in order to compare the differential gas release. Analytical procedures followed Villa et al. (2000). Cd shielding was avoided during irradiation so as not to lose the information on release of Cl-derived ^{38}Ar. The released gas was purified using SAES C50 and AP10 getters, and the argon isotopic composition was measured on a Faraday cup using an MAP 215-50B mass spectrometer, operated in peak-jumping mode between masses 35.5 and 40.6. Peak heights were extrapolated back

to inlet time. Final data were corrected for mass spectrometer background, blank, mass discrimination (0.12%/a.m.u.), post-irradiation decay of ^{37}Ar and neutron-induced interferences ((^{39}Ar/^{37}Ar)$_{Ca}$ = 0.00067, (^{36}Ar/^{37}Ar)$_{Ca}$ = 0.000255, (^{40}Ar/^{39}Ar)$_K$ = 0.015, (^{38}Ar/^{39}Ar)$_K$ = 0.013, (^{38}Ar/^{37}Ar)$_{Ca}$ = 0.000027). Ar-isotope in Table 2 (electronic supplement) data were corrected for blank, discrimination and post-irradiation decay of ^{37}Ar. Average blanks were 2 pl ^{40}Ar below 1,000 °C and rose to 6 pl ^{40}Ar in the final extraction step; they were higher than in Villa et al. (2000). Step duration was between 20 and 40 min. Ca/K ratios were calculated from ^{37}Ar$_{Ca}$/^{39}Ar$_K$ ratios using a production efficiency correction factor of 1.98, whereas Cl/K ratios were calculated from ^{38}Ar$_{Cl}$/^{39}Ar$_K$ ratios using a correction factor of 0.23. Only PEI26 was irradiated in a different reactor position and had a correction factor of 0.44. The Cl production rate was determined from wet chemical analyses of the irradiation monitor FCT biotite (Villa et al. 2000). For laser-ablation ^{40}Ar/^{39}Ar, the factors for Ca/K and Cl/K ratio calculation were 2.01 and 0.23 respectively.

Laser-ablation ^{40}Ar/^{39}Ar

Laser-probe and stepwise-heating experiments enable comparison of the different information provided by the two techniques, namely, high spatial-resolution analyses for the laser probe vs. differential gas release from chemically/mineralogically distinct phases during stepwise heating. The close association of non-resorbed clasts and intervening matrix within pseudotachylytes demands a high spatial-resolution technique in order to contrast the isotopic signature of older clasts from visually clast-free melt zones. In order to perform in-situ analyses, thin slices of each sample (~7×7×0.1 mm) were prepared and polished on one side. Except for samples JAU34A and PEI26, SEM backscattered electron image maps were acquired prior to irradiation to provide detailed control for the location of future analyses. Before being wrapped in aluminium foil, the carbon coating was polished off and the samples were ultrasonically cleaned in methanol. The samples were irradiated without Cd shielding at the Risø reactor (Denmark), along with biotite GA1550 (97.9 Ma; McDougall and Roksandic 1974) and biotite "tinto" (410.3 Ma; Rex and Guise 1986). Following irradiation, the samples were loaded into an ultra-high vacuum laser port with polished sides up and heated using a heat lamp overnight to reduce atmospheric argon from sample surfaces; pre-ablation was not used. The laser system consisted of a Spectron SL902 TQ CW Nd YAG laser (1,064 nm) running at 15–17 W connected to an external computer-controlled shutter. The sample was observed using a CCD camera mounted on a Leica Metallux 3 microscope, through which the laser beam was also directed onto the sample surface. In order to avoid heating of adjacent clasts and excessively deep penetration into the pseudotachylyte sample and consequent loss of resolution, 5 to 15 individual shots of 5- to 20-ms duration were performed, generally ablating less than ~0.5 mm^2 for each analysis. Depth of IR laser pits was 50–100 μm. The size of the area ablated was not limited by the spatial resolution of the IR laser but by the amount of released argon necessary to ensure a precise measurement for the relatively young samples considered. The gas released was purified using two SAES AP10 getters (one held at 450 °C and one at room temperature) for 5 min and expanded into an MAP 215-50 mass spectrometer utilising a Balzers SEM operated in analogue mode. Masses 35 (chlorine), 36–40, and 41 (hydrocarbon) were measured ten times by peak jumping; peak heights were extrapolated back to inlet time. Blanks were run after every two sample analyses. Blank corrections for all Ar isotopes were mainly based on daily averages or sometimes also linear curve fits, when a slight increase in blank levels was observed during the course of the day. In general, blank levels varied little (8–20%, 1σ s.d.) and averaged 2.5×10^{-12}, 0.04×10^{-12} and 0.05×10^{-12} ml for ^{40}Ar, ^{39}Ar and ^{36}Ar respectively. Final data in Table 3 (electronic supplement) were corrected for mass spectrometer discrimination, ^{37}Ar decay and neutron interferences ((^{39}Ar/^{37}Ar)$_{Ca}$ = 0.00067, (^{36}Ar/^{37}Ar)$_{Ca}$ = 0.000255, and (^{40}Ar/^{39}Ar)$_K$ = 0.045 determined from pure CaF$_2$, K$_2$SO$_4$, and KCl).

Rb–Sr microsampling

As (sub)-mm lithological banding resembling features in Thöni (1988) was observed in some investigated pseudotachylytes (PEI12, JAU10), Rb–Sr microsampling was used to analyse individual layers directly extracted from polished thick sections (~60 μm) using a microdrill (Müller et al. 2000a). Sample weights ranged from ~50 to ~500 μg, except for JAU10/1, 10/2 and 10/4 (5–15 mg) which were initially prepared using the same core drill as for stepwise-heating ^{40}Ar/^{39}Ar samples. Analytical details of Rb–Sr microsampling techniques are in Müller et al. (2000a).

Constants used are those from Steiger and Jäger (1977). All quoted errors are 95% c.l., unless where otherwise stated.

Electron microprobe analyses (EMPA)

Quantitative chemical analyses of pseudotachylyte matrix and clasts were performed on separate thin sections using a Cameca SX-50 electron microprobe equipped with five crystal spectrometers and operated with 15-kV accelerating voltage and 20-nA sample current. Samples were coated with ~20 nm of carbon. Standards were both natural and synthetic silicates and oxides. Raw data were corrected for drift, dead time and background; the ZAF correction of Pouchon and Pichoir (1984) was applied to the data. Given the small grain size of pseudotachylyte matrices, the location of analyses was determined using BSE images to avoid mixed analyses as far as possible. Raster analyses were often performed to obtain an average value for a chosen area.

Scanning electron microscope (SEM)

A CamScan CS44 SEM equipped with a LaB$_6$ filament and operated with 15-kV accelerating voltage was used to obtain BSE images for laser ^{40}Ar/^{39}Ar work. Working distance was 15 mm for images and 35 mm for EDX qualitative analyses.

Geological framework and sample description

The samples analysed were collected from the Peio, Jaufen and Tonale faults, all part of the Periadriatic (Insubric) Fault System (PAF; e.g. Schmid et al. 1989; Müller et al. 2001). The PAF dissects the whole Alps in an approximately E–W direction for over ~700 km (Fig. 1). It forms a first-order tectonic boundary between Penninic and Austroalpine units characterised by variable degrees of Alpine, i.e. Cretaceous or Tertiary, metamorphism to the north(west), and South Alpine units to the south(east) which are virtually unaffected by Alpine metamorphism (e.g. Schmid et al. 1989). Several models have been published for the evolution of this complex fault system, depending on the assigned age of fault activity of the various faults involved (for a review see Müller et al. 2001). Clearly, accurate "fault ages" of the above mentioned faults are needed in order to establish an internally consistent tectonic model.

The Peio and Jaufen faults are both intra-Austroalpine faults located immediately north of the Periadriatic fault s. str. (Fig. 1). Both faults separate northern basement units characterised by Eo-Alpine (Cretaceous) metamorphism from Alpine, weakly overprinted high-grade gneisses to the south (Thöni 1981; Del Moro et al. 1982; Martin et al. 1991; Werling 1992; Spiess 1995). The Peio fault separates the Campo crystalline unit

characterised by heterogeneous, low-grade Cretaceous greenschist facies metamorphism from weakly over-printed, pre-Alpine high-grade gneisses of the Tonale-Ulten unit. From the distribution of mylonites, pseudotachylytes and cataclasites, the dip of foliation planes and stretching lineations as well as various kinematic indicators, sinistral normal faulting along the Peio fault has been deduced (e.g. Werling 1992).

Pseudotachylyte and ultramylonite samples PEI49, PEI52 and PEI53 were collected from one outcrop within the immediate foot wall of the Peio fault (Fig. 1). The two pseudotachylyte fault veins and the mylonitic foliation of PEI53 are parallel to the main Peio fault plane. The three samples are spaced by only ~5 m in altitude. Dark "pseudotachylyte clasts" which resemble sigma-type porphyroclasts can be observed within the mylonites of the Peio fault (Müller et al. 2001). They indicate top-to-ESE displacement consistent with other shear criteria for the Peio fault. Contemporaneity between mylonites and pseudotachylytes is thus inferred on the basis of mutual overprinting relationships. Pseudotachylyte PEI49 is a black, 2–3 cm thick fault vein (Fig. 2a; see Table 1 for further petrographic details). Pseudotachylyte PEI52 is a ~7-cm-thick, dark grey pseudotachylyte fault vein with pronounced, ~0.5-cm-thick, black finer-grained margins resembling chilled margins (Fig. 2b, Table 1). When sampled in the field, ultramylonite PEI53 was also considered to represent a pseudotachylyte vein because of its black vein-like appearance. However, in thin section it turned out to be a very fine-grained ultramylonite–phyllonite, generated by virtually complete, hydrolytically induced breakdown (e.g. Kronenberg et al. 1990) and recrystallisation of the original mineral assemblage (Fig. 2c, Table 1).

Immediately to the south of the Peio fault, slightly more steeply dipping (>25°), discrete, low-temperature shear zones are characterised by pseudotachylytes and fine-grained mylonites to phyllonites which were originally interpreted to be cogenetic with the Peio fault (Werling 1992). On the basis of top-to-(W)NW kinematics, which is effectively opposite to the main Peio fault, and recently obtained fission-track ages, these thrusts must be regarded as a separate kinematic event (Martin et al. 1991; Viola 2000). Pseudotachylytes PEI12 and PEI26 and mylonites PEI27 and PEI33 were collected along these low-grade shear zones south of the Peio fault in order to establish the age of this distinct kinematic event relative to the main Peio fault. Pseudotachylyte

Fig. 2a–f. Photomicrographs of samples related to the Peio fault (s.l.). **a** High-resolution SEM backscattered image of PEI49. Tiny biotite laths (*bio*) are randomly oriented and embedded in a plagioclase (*plag*) matrix, resembling magmatic textures. Quartz (*qtz*) clasts have thin rims of ?K-feldspar (*kfsp*). **b** Up to 7-cm-thick pseudotachylyte fault vein PEI52 showing characteristic chilled margins. **c** Ultramylonite PEI53 showing small-scale layering of dynamically recrystallised quartz, fine-grained plagioclase and white mica. **d** Quartz (*qtz*) clasts showing strong resorption phenomena (*arrows*) within pseudotachylyte PEI12. **e** Specimen of fault and injection vein of pseudotachylyte PEI26. Fault veins are parallel to the mylonitic foliation. **f** Similar layering as in **c** for orthogneiss mylonite PEI33 (crossed polarisers)
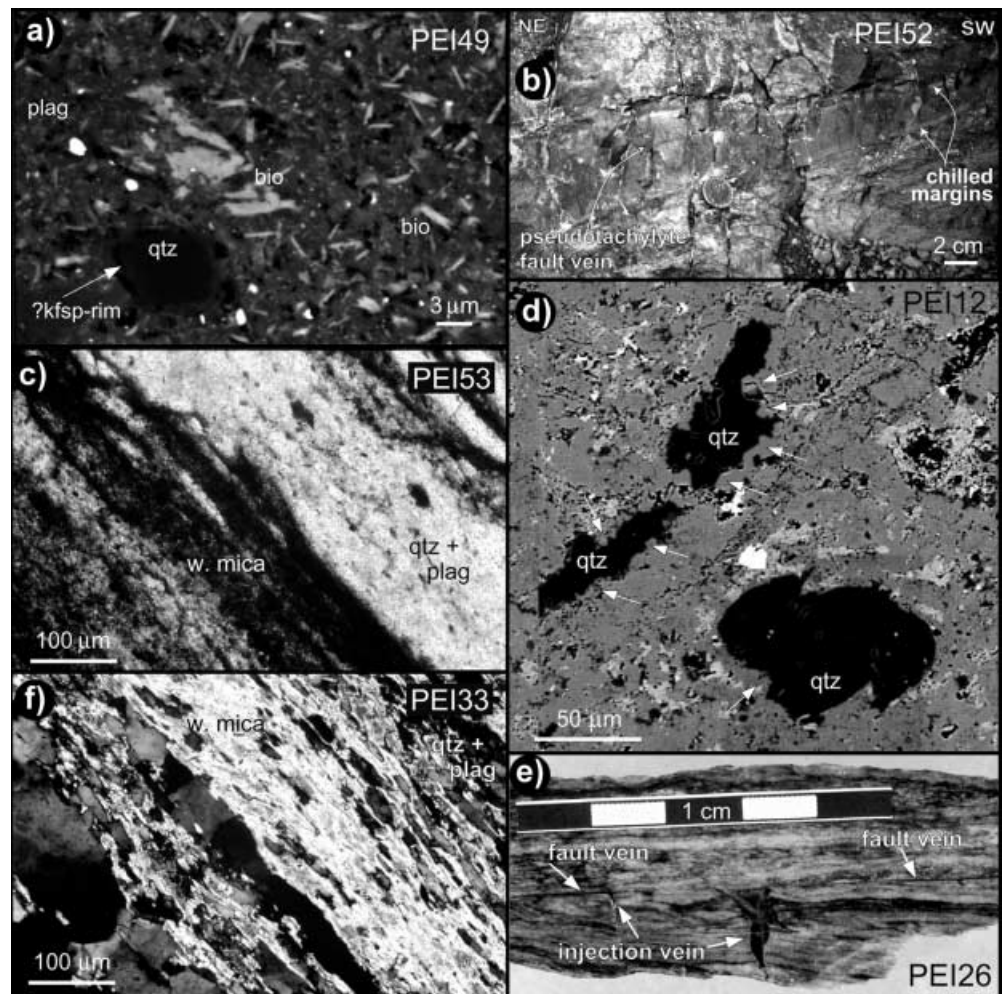
Table 1. Summary of petrographic features and related chemistry of analysed pseudotachylytes (*pst*) and (ultra)mylonite (*myl*) samples

Sample	Location	Macroscopic description	Clast mineralogy	Matrix mineralogy and texture (partly revealed using high-resolution BSE imaging)	EMPA-derived matrix chemistry	[40]Ar/[39]Ar-derived matrix chemistry
PEI49 (pst)	Peio fault, Le Cocchiole	Black fault vein parallel to strike of Peio fault, 2–3 cm thick	Numerous, variably rounded and partially resorbed quartz, low-Ca plagioclase, lithic clasts (include also rare biotite, < 50 μm); size of clasts between < 50 μm and rarely ∼1 mm	Randomly oriented, tiny biotite laths (< 2 μm) embedded in a very fine-grained plagioclase matrix, resembling a magmatic texture (Fig. 2a); quartz clasts contain thin rims of plagioclase which tend to seal resorption bays	Ca/K: 0.2–0.55, clustering 0.3–0.4; Cl/K: ∼0.005; K: 3.6% (5×5 μm raster)	Ca/K: mostly 0.3–0.4 (0.2–0.55); Cl/K: 0.004–0.007; K: 3.2% (stepwise-heating; effect of clasts has to be taken into account)
PEI52 (pst)	Peio fault, Le Cocchiole	Dark grey fault vein parallel to strike of Peio fault, 7 cm thick with 0.5-cm black, finer-grained margins resembling chilled margins (Fig. 2b), thin undeformed injection veins along host-rock contact	Numerous, variably rounded and partially resorbed clasts, mostly 100–400 μm, rarely up to 2 mm, composed of dynamically recrystallised quartz fragments (?mylonitic precursor) and rare plagioclase	Brown, crystalline matrix, parallel fabric (?flow structure) along chilled margins, textureless towards the centre of the vein; 5–10 μm, randomly oriented biotite needles (partly spherulites nucleating at small clasts) within non-resolvable matrix (?feldspar); along cracks, incipient bleaching	n.a.	Pristine melt: Ca/K: 0.1–0.25; Cl/K: 0.002–0.003; K: 3.2%
PEI53 (myl)	Peio fault, Le Cocchiole	5-cm thick (ultra)mylonite, black; in outcrop resembling a pseudotachylyte fault vein	Only very few, large white mica and albite clasts (> 100 μm)	Layers mm-thick, alternatingly composed of fine-grained (< 5 μm) white mica, quartz, albite; generated by hydrolytically induced breakdown of the precursor mineralogy (large albite, white mica and quartz; Fig. 2c)	n.a.	n.a.
PEI12 (pst)	Shear zones S of Peio fault, Forcellina di Montozzo	≤ 1 cm thick, black injection veins intruding the host rock, a low-temperature protomylonite (plagioclase, K-feldspar, strongly dynamically recrystallised quartz ribbons (< 10 μm), clinozoisite, ± white mica)	Mylonitic quartz ribbons and plagioclase (< 100 μm); strong resorption of quartz clasts by the pseudotachylyte melt (Fig. 2d), a significant increase of matrix SiO$_2$ and a concomitant decrease of K$_2$O is observed in resorption bays of quartz clasts	Two different matrix domains: (1) channel-like structures with no textural heterogeneity even at the (sub-)μm-scale, having K-feldspar composition; (2) K-feldspar matrix with small (< 4 μm), randomly oriented Si-Al-Fe-Mg-laths (?chlorite)	Ca/K: average 0.035 (0–0.08, the latter close to clasts); Cl/K: ∼0.0003–0.0008; K: 10.3%, mineral chemical composition resembling K-feldspar (Table 1 in electronic supplementary material)	Ca/K: 0.02–0.026; Cl/K: 0.00015–0.0003; K: 9.5% (effect of clasts has to be taken into account)

Table 1. (Contd.)

Sample	Location	Macroscopic description	Clast mineralogy	Matrix mineralogy and texture (partly revealed using high-resolution BSE imaging)	EMPA-derived matrix chemistry	$^{40}Ar/^{39}Ar$-derived matrix chemistry
PEI26 (pst)	Shear zones S of Peio fault, Forcellina di Montozzo	~7-mm-wide and 20-mm-long injection vein crosscutting (ultra)mylonite/ phyllonite PEI27; pseudotachylyte is generated as fault vein along a thin (<0.3 mm), foliation-parallel fault plane (Fig. 2e)	Rounded and partially resorbed clasts of dynamically recrystallised quartz ribbons (<500 μm), rare albite and epidote	Textures indicative of melt flow; 0.5–1 mm wide chilled margins; along these margins, the matrix appears to be more strongly (re-)crystallised to a network of fine-grained white mica and plagioclase (~10 μm) whereas fewer and smaller (<5 μm) white mica (?) laths are present in the centre of the vein	Ca/K: average ~0.12 (0.02–0.25); Cl/K ratios: 0.006–0.05 (?); raster mode K: average ~4.5% (10×10 μm raster); matrix areas with significantly lower K levels also occur	Ca/K: ~0.03–0.25; K: 2.8% (stepwise-heating $^{40}Ar/^{39}Ar$); Cl/K ratios: ~0.002–0.008
PEI27 (myl)	Shear zones S of Peio fault, Forcellina di Montozzo	Host rock of pseudotachylyte PEI26; very strongly foliated, resembling an ultramylonitic or phyllonitic fabric	Only very few, large white mica (>100 μm), no albite clasts in (ultra)phyllonitic domains; porphyroclasts were avoided during microsampling	Original paragenesis of medium- to fine-grained white mica, albite and quartz is locally completely retrogressed (hydrolytically weakened) to very fine-grained (<5 μm) white mica and quartz-rich layers	n.a.	n.a.
PEI33 (myl)	Shear zones S of Peio fault, Forcellina di Montozzo	Strongly foliated orthogneiss–mylonite with dynamically recrystallised quartz ribbons and fine-grained biotite and white mica	Porphyroclasts: plagioclase, K-feldspar, biotite and white mica, all showing variable degrees of partial breakdown (clinozoisite needles in plagioclase, sericitisation of feldspars and exsolution of oriented TiO_2 lamellae in biotite)	Very localised, virtually complete breakdown of the magmatic mineral assemblage into fine-grained quartz, biotite and white mica, which has been utilised for Rb–Sr microsampling (Fig. 2f)	n.a.	n.a.
JAU10 (pst)	Jaufen fault, creek ~1.5 km SW Jaufen pass	Brown, clast-laden, ~5 mm thick fault vein with minor injections into the host rock; host rock is retrograde, quartz-rich orthogneiss (quartz, K-feldspar, plagioclase, white mica and biotite)	Numerous, rounded clasts showing different degrees of resorption by the melt; clasts composed of strongly undulose quartz, with subordinate lithic clasts (quartz aggregates) and feldspar (grain sizes <800μm); quartz from the pseudotachylyte–wall rock contact is partially resorbed and shows concave grain boundaries towards the matrix/melt	Shows (melt) flow textures; matrix is composed of an anastomosing network of fine-grained (<3 μm) biotite (?) along the contact to the host rock, interpreted to reflect incipient recrystallisation; finer-grained and pristine matrix occurs in the centre of the veins	n.a.	Two different sample aliquots: K: 3.6 and 3.1% respectively; Ca/K: ~0.02–0.04; Cl/K: ~0.0005

Table 1. (Contd.)

Sample	Location	Macroscopic description	Clast mineralogy	Matrix mineralogy and texture (partly revealed using high-resolution BSE imaging)	EMPA-derived matrix chemistry	$^{40}Ar/^{39}Ar$-derived matrix chemistry
JAU34A (pst)	Jaufen fault, creek ~1.5 km SW Jaufen pass	Black fault vein, ~8 mm thick; host rock: retrograde, quartz-rich orthogneiss (quartz, K-feldspar, plagioclase, white mica and biotite), similar to JAU10	Mainly rounded quartz (< 400 μm) and subordinate plagioclase clasts	Less strongly (re-) crystallised matrix when compared to JAU10, except along the wall-rock contact (Fig. 3a); in the centre of the vein, the pristine matrix is very fine-grained and cannot be resolved optically; secondary bleaching of the pseudotachylyte matrix along joints is common; a second thin pseudotachylyte generation intrudes the matrix of the first, presumably indicating recurrent seismic (?) activity	Ca/K: 0.03–0.08 (10×10 μm raster); Cl/K: low, 0.001–0.002, with Cl close or at the detection limit; K: 4.7%	Ca/K: ~0.05–0.15; Cl/K: ~0.0010–0.0016 (step); –0.005 (laser); K: 3.1% (stepwise-heating $^{40}Ar/^{39}Ar$ analyses)
TO27 (pst)	Anti-Riedel N of eastern Tonale fault, Pellizano	Injection vein, < 4 mm wide (Fig. 3b), hosted by a retrogressed, relatively fine-grained paragneiss (Tonale unit), consisting of sericitised plagioclase, white mica, quartz, chlorite, minor biotite and apatite	Predominantly quartz (or lithic clasts comprised of ribbon quartz) and rare plagioclase; virtually all show resorption phenomena along their contacts to the melt	Melt inflow into the injection vein is recorded by aligned matrix minerals subparallel to the pseudotachylyte margins (Fig. 12a); fully crystallised matrix with a relatively coarse-grained assemblage of predominantly albite, chlorite (?) and rare biotite (average grain size ~10 μm), all having interlocking textures which resemble magmatic textures; matrix minerals are more randomly oriented towards the centre of the vein, interpreted as primary crystallization feature; along the sharp wall-rock contacts, an ~100 μm wide, finer-grained matrix occurs (chilled margins?;Fig. 3c)	Analyses of primary chlorite (?) and albite with interlocking "magmatic" textures (Table 1 in electronic supplementary material)	Only laser-ablation $^{40}Ar/^{39}Ar$; Ca/K: ~0.2–3; Cl/K: ~0.0005–0.0025 (correlated with apparent age)

PEI12 shows black, < 1 cm thick injection veins intruding the host rock, which is a low-temperature protomylonite (Fig. 2d, Table 1). PEI12 has the highest potassium concentration of any of the samples (~10%) and a chemical composition which resembles K-feldspar (see Table 1 in electronic supplementary material). Pseudotachylyte PEI26 is an ~7-mm-wide and 20-mm-long injection vein (Fig. 2e, Table 1) crosscutting an (ultra)mylonite–phyllonite, referred to as PEI27 (see below) and which shows top-to-WNW sense of shear. Since the pseudotachylyte is generated along a narrow (< 0.3 mm), foliation-parallel fault plane, both mylonites and pseudotachylytes are interpreted to be contemporaneous and to reflect similar kinematics. Low-grade mylonite–phyllonite PEI27 was

sampled at a distance of ∼0.5 m from PEI26. An original paragenesis of medium- to fine-grained white mica, albite and quartz is locally completely retrogressed to very fine-grained (< 5 µm) white mica and quartz resembling an ultramylonitic or phyllonitic fabric. The second sample from the southern mylonite zone is a strongly foliated orthogneiss mylonite, referred to as PEI33, which shows a deformationally induced, localised (mm-scale), virtually complete breakdown of the original magmatic mineral assemblage into fine-grained quartz, white mica and biotite (Fig. 2f, Table 1).

The boundary between the Ötztal crystalline unit characterised by Upper Cretaceous, amphibolite facies metamorphism to the north and the Alpine weakly metamorphosed Meran-Mauls basement to the south is represented by the Jaufen fault (Fig. 1; Spiess 1995). Two major kinematic events have been recognised along the Jaufen fault according to Glutz (1997) and Parolini (1997): (1) a steeply NW-dipping mylonitic foliation with sinistral and south-side-up sense of displacement discordantly cuts a Late Cretaceous foliation; temperature conditions of deformation have been estimated to be ∼300–350 °C; (2) a second, dextral, semiductile to brittle deformation occurred along steeply dipping fault planes with subhorizontal lineations, producing low-T mylonites, pseudotachylytes and cataclasites. Two pseudotachylytes from one large outcrop hosted by an orthogneiss (JAU10 and JAU34A) related to the second kinematic event have been investigated (Fig. 3a; Table 1).

The Tonale and Pusteral faults represent roughly E–W-trending segments of the Periadriatic fault s. str., connected via the N(N)E-trending Giudicarie-Mauls fault (for a review see Schmid et al. 1989; Müller et al. 2001; Fig. 1). Along the eastern Tonale fault, dextral strike-slip displacement prevails (Werling 1992), in contrast to the western section where also vertical movements related to the exhumation of the northern Penninic zone occur (e.g. Schmid et al. 1989). Frequent Oligocene plutons and thin intrusive "lamellae" (∼30–32 Ma; e.g. Bregaglia/Bergell, Adamello-Presanella, Samoclevo-Rumo, Mauls, Lesachtal) represent excellent time markers for the evolution of the Tonale-Pusteral faults and demonstrate syn- to post-intrusive formation of mylonites and rare pseudotachylytes. One pseudotachylyte, TO27, was collected at an outcrop immediately north of the eastern Tonale fault (Fig. 1). Because of the (N)NW-trending orientation of these fault planes and their sinistral sense of shear, these faults are interpreted as antithetic Riedel shears to the dextral Tonale fault (Table 1; Müller et al. 2001). The pseudotachylyte was generated along thin fault planes subparallel to the foliation (fault vein), and intrudes the host rock effectively perpendicular to its foliation (injection vein, Fig. 3b, c).

Results

Results obtained from seven pseudotachylytes and three cogenetic (ultra)mylonites are listed in Tables 1, 2, 3 and
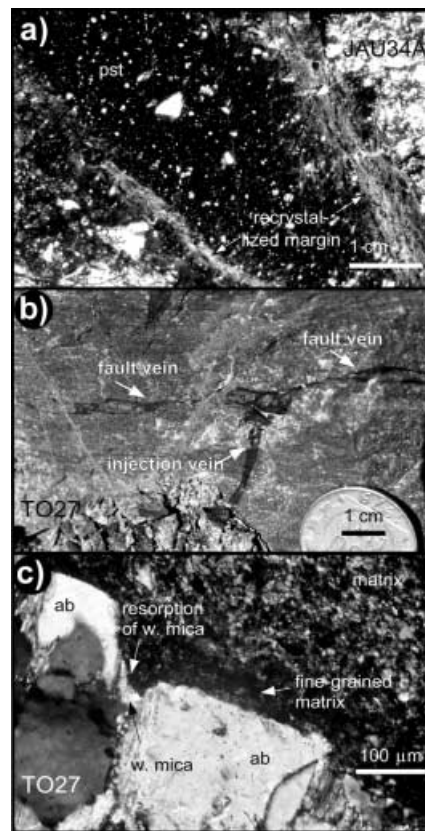

Fig. 3a–c. Photomicrographs of pseudotachylytes from the Jaufen and Tonale faults. **a** Photomicrograph of pseudotachylyte JAU34A showing thin zones of incipient recrystallisation of the pristine pseudotachylyte matrix along the host-rock contacts. **b** Outcrop photograph of fault and injection vein TO27, the latter crosscutting the host-rock foliation. **c** Photomicrograph of the contact of the pseudotachylyte injection vein to the host rock of TO27 where fine-grained chilled margins are developed. White mica (*w. mica*) of the host rock is preferentially resorbed compared with adjacent albite (*ab*; crossed polarisers)

4 in electronic supplementary material and displayed in figures below (see Table 1 for petrographic descriptions as well as chemical characteristics, and the Appendix for sample locations). Most pseudotachylytes have been analysed by more than one dating technique in order to compare results of different techniques, thereby controlling the validity of results. Combined stepwise-heating and laser-ablation $^{40}Ar/^{39}Ar$ analyses are reported for pseudotachylytes JAU34A, PEI26, and PEI49, whereas combined stepwise-heating $^{40}Ar/^{39}Ar$ and Rb–Sr microsampling analyses have been performed on JAU10 and PEI12. PEI52 and TO27 have been analysed only by stepwise-heating and laser-ablation $^{40}Ar/^{39}Ar$ analyses respectively. Regarding the comparison of results obtained by different techniques, it is important to keep in mind that pseudotachylytes are likely to show some chemical heterogeneity on the mm-scale (e.g. Kelley and Spray 1997), due to their short-lived formation process. This inevitably poses a limit for direct comparison, especially of chemical information, as the different techniques operate on different scales

and places of the same samples (e.g. drill cores for step heating vs. in-situ laser spots). Ar (and hence ages) are likely to be reset by volatile loss (see below), whereas diffusional equilibration of non-volatile species following frictional melting is too slow to achieve chemical homogeneity for an entire pseudotachylyte.

Rb–Sr microsampling analyses of (ultra)mylonites from the same outcrops (PEI53 in the case of pseudotachylytes PEI49 and PEI52) or fault zones (PEI27 and PEI33 in the case of pseudotachylytes PEI12 and PEI26) help to independently evaluate the pseudotachylytes ages. Eleven additional pseudotachylyte ages from the PAF have been presented in Müller et al. (2001).

Jaufen fault

Two pseudotachylytes (JAU10 and JAU34A) were collected in close mutual proximity (∼100 m distance) in the same sector of the Jaufen fault; JAU10 was sampled in situ and JAU34A was a loose block. Pseudotachylyte JAU34A was analysed both by stepwise-heating and laser-ablation $^{40}Ar/^{39}Ar$. A staircase age spectrum with ages mostly between 20 and 40 Ma (extremes ranging between 6 and 500 Ma) was recorded during step heating (Fig. 4a). Distinct peaks in Ca/K and Cl/K spectra at low and intermediate temperatures suggest argon release from specific, young mineral phases, which we attribute to alteration and which may have been contained in microscopic cracks of the drill cores. Steps 10–13 record older ages. It is important to make a rigorous distinction between data presentation formats. Age, Ca/K and Cl/K spectra, such as those displayed in Fig. 4a, are more readily understandable, but they may mislead on the detailed identification of the different Ar reservoirs. The only way to ascertain the chemical identity of an Ar reservoir is via correlation diagrams, such as Fig. 4b, c. In the following all our identifications of melt-related steps will be based on the corners of polygons in such diagrams (e.g. Villa 2001). When plotted into a Ca/K–Cl/K diagram, two clusters of steps are visible (Fig. 4b). Low Ca/K–Cl/K ratios characterise melt-related steps, which is in line with EMPA analyses, whereas elevated Ca/K–Cl/K ratios are indicative of clasts and/or alteration-related phases. This also matches laser-spot analyses performed on melt or clast areas (see below). One corner of the polygon defined by the data points is closest to step 6 (and 10), which are therefore identified as closest representatives of the original melt; their ages are 19.4 (and 21.4) Ma. Two divergent mixing trends pointing towards both clast and alteration phases are revealed in an apparent age–Ca/K diagram, with the melt composition (step 6) lying on their intersection (Fig. 4c).

Fifteen individual laser-spot ages were analysed from a thick section prepared from the least altered, interior parts of JAU34A (Fig. 3a). When plotted on an isochron diagram, two tight clusters of analyses can be distinguished (Fig. 4d). Limiting ourselves to analyses on
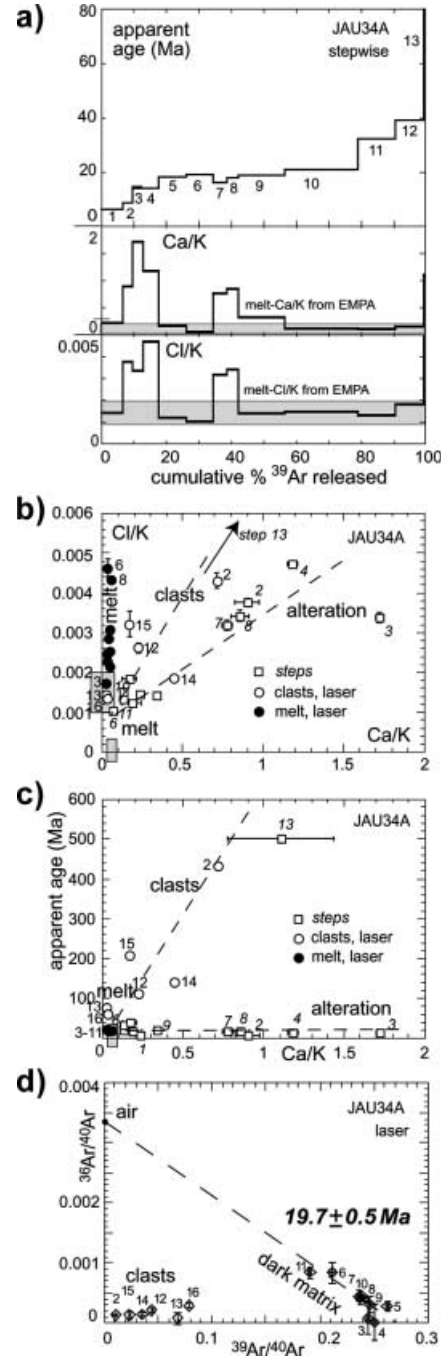

Fig. 4a–d. Jaufen fault pseudotachylyte JAU34A. **a** $^{40}Ar/^{39}Ar$ stepwise-heating spectra. **b** Cl/K–Ca/K plot; *shaded areas* denote the range of corresponding, melt-related EMPA analyses. **c** Age–Ca/K plot of both step-heating and laser-spot $^{40}Ar/^{39}Ar$ analyses. **d** Laser-spot isochron plot (for a discussion of the discrimination plots, see Villa et al. 2000, and Villa 2001). The pseudotachylyte melt lies at the intersection of mixing trends towards clasts and alteration. The errors of the step-heating Cl/K and Ca/K ratios are often smaller than the size of the plot symbol

Ca-poor spots (Fig. 4b), the weighted mean age of analyses performed within dark matrix domains lacking clasts (#3–11) is 19.7 ± 0.5 Ma, with no indication of any non-atmospheric $^{40}Ar/^{36}Ar$ component. Ca/K ratios of

these spots calculated from reactor-produced isotopes range from 0.025 to 0.05 (mean 0.04), which is in line with Ca/K ratios of matrix domains measured with the microprobe. Corresponding Cl/K ratios (0.0017–0.0046) are mostly higher than those of matrix-related steps and EMPA analyses, but neither reveal any correlation with age or Ca/K. Hence, the slab used for laser-spot dating most probably contained more Cl but none of the few, alteration-filled cracks which were unavoidably present in the step-heating sample. Cl contamination due to polishing can be ruled out, since not all samples show this effect but were prepared in the same way. Similar chemical inhomogeneities on the < 10 mm scale have been observed by Kelley and Spray (1997) and appear to be a characteristic feature of pseudotachylytes. Six other laser-spot analyses have been performed on big clasts (quartz, feldspar) or very close to the host rock (#13, 16), and they show low $^{39}Ar/^{40}Ar$ ratios. They record apparent ages between 60 and 430 Ma and varying Ca/K ratios (up to 0.75). They match clast-related steps from step-heating experiments and demonstrate the capability of high spatial-resolution analyses in resolving different ages and chemical components within one thick section.

Both stepwise-heating $^{40}Ar/^{39}Ar$ and Rb–Sr microsampling analyses were performed on JAU10. Since ~90% ^{39}Ar was unexpectedly released during the first three steps of the first stepwise-heating experiment, a second analysis of an independently irradiated sample was conducted to achieve a better resolution (JAU10/II). The two age, Ca/K and Cl/K spectra are very similar (Fig. 5a). Low- to intermediate-temperature steps are characterised by very low Ca/K ratios, whereas a significant increase in Ca/K is observed at highest experimental temperatures. This coincides with both increasing Cl/K ratios and older ages, and points to partially resorbed plagioclase (and quartz?) inherited from the host rock. Very low Cl/K ratios and younger ages, possibly indicating the presence of a later alteration phase, consistently characterise the first steps of both age spectra. Because steps 2 to 5 of JAU10/II (63% ^{39}Ar released) plot closest to the intersection between the alteration and clast-related mixing trend, they can be used to calculate a weighted mean age of 16.5 ± 0.8 Ma. Unlike JAU34, young alteration minerals have low Cl/K ratios in this sample. One should view aqueous alteration processes from the perspective of fluid-inclusion research, because the latter can provide the sequence as well as the chemistry of fluids which have circulated through a given rock. Fluid-inclusion studies show that there is no one-for-all rule, and late inclusions can be both more saline and less saline than early ones. It appears to be unpredictable whether a fluid forming an alteration mineral has a higher or a lower Cl/K ratio than the predecessor minerals.

Rb–Sr (microsampling) analyses were conducted on three drill cores similar to those used for stepwise-heating experiments, and four microsamples prepared from adjacent, lithologically different layers in thick section (sample weights between 49 and 358 μg, altogether
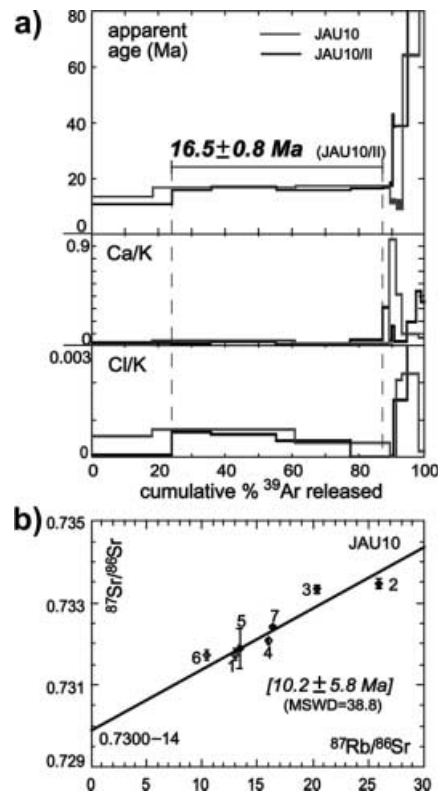

Fig. 5a, b. Jaufen fault pseudotachylyte JAU10. **a** $^{40}Ar/^{39}Ar$ stepwise-heating spectra (two separate irradiations); Cl/K values have been set to zero, where Cl values calculated from ^{38}Ar were (slightly) negative. **b** Rb–Sr (microsampling) isochron diagram

comprising an area of ~15 mm^2). The overall variation in $^{87}Rb/^{86}Sr$ among the seven samples is 10.4 to 25.9, and is more limited among the four microsamples (10.4–16.3; JAU10/4–7). Plotted on an isochron diagram (Fig. 5b), all seven samples scatter around a reference line whose slope corresponds to an "age" of 10.2 ± 5.8 Ma (MSWD = 38.9). If only the four, spatially close microsamples are regressed together, an "age" of 8 ± 11 Ma ($2\sigma_{ext.}$) is indicated. Because of the strong scatter of the data points even on a scale of ~5 mm, all these "ages" are geologically meaningless, due to the lack of Sr isotopic homogenisation during pseudotachylyte formation and additional later alteration.

Shear zones south of the Peio fault

Pseudotachylytes PEI12 and PEI26 as well as mylonites PEI27 and PEI33 were collected from shear zones in the hanging wall immediately south of the Peio fault. Pseudotachylyte PEI12 was analysed both by stepwise-heating $^{40}Ar/^{39}Ar$ and Rb–Sr microsampling. The apparent age spectrum of PEI12 shows smoothly increasing ages from 35 to 41 Ma at low- to intermediate-temperature steps (Fig. 6a). Because of the obvious positive correlation between ages, Ca/K, and Cl/K (Fig. 6b), the linear trend in all three correlation
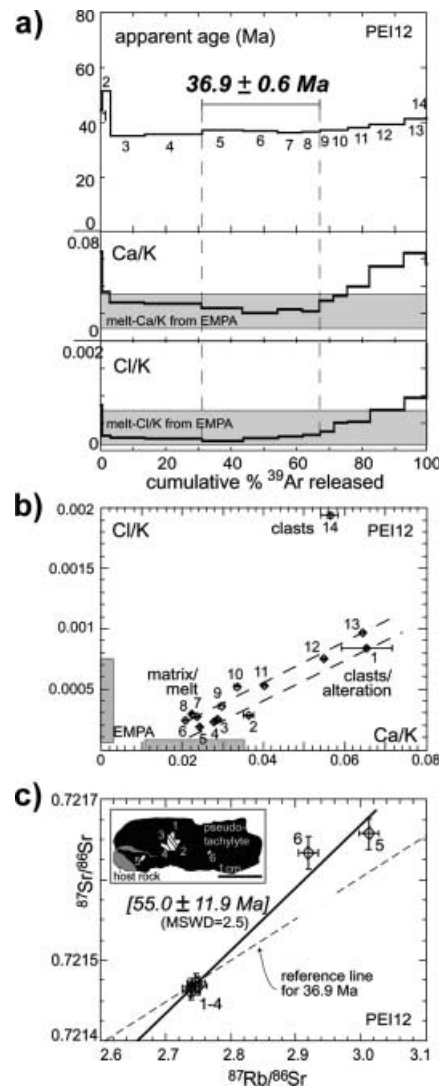
Fig. 6a–c. Pseudotachylyte PEI12, collected along a shear zone south of the Peio fault. **a** $^{40}Ar/^{39}Ar$ stepwise-heating spectra. **b** Corresponding Cl/K–Ca/K plot based on Ar isotopes. **c** Rb–Sr microsampling isochron diagram; the *inset* shows a sketch of the thick section used for the preparation of the microsamples, whose location is indicated by open *numbered areas* (see text for details)

High-temperature steps record slightly older ages which coincide with higher Ca/K and Cl/K ratios, most probably related to incompletely degassed plagioclase/quartz clasts. Ages older than ~50 Ma recorded in the first two steps are possibly the result of degassing of alteration-related excess-^{40}Ar-bearing minerals.

Rb–Sr microsampling dating was attempted because PEI12 shows weakly developed lithological layering on the (sub-)mm scale. Four samples (1–4) devoid of clasts or cracks were cut out parallel to the layering adjacent to each other (see inset in Fig. 6c; sample weights between 178 and 512 µg, altogether comprising ~6 mm²). Both their Rb and Sr concentrations and $^{87}Sr/^{86}Sr$ ratios are very similar, precluding any age determination but demonstrating that the pseudotachylyte-forming event produced a homogeneous melt with respect to Rb and Sr at the mm²-scale (Fig. 6c). In order to check whether any variation occurs on the scale of a thick section, two additional microsamples were analysed. Sample 5 was excised from a narrow injection vein enclosed by the host rock. The resulting $^{87}Rb/^{86}Sr$ and Sr isotopic ratios are slightly different from those recorded for samples #1–4. However, the limited spread in Rb/Sr ratios, and the fact that sample 5 stems from a narrow injection vein which is likely to be out of equilibrium with the main vein preclude a reliable age calculation. The "age" of ~55 Ma is geologically meaningless.

Pseudotachylyte PEI26 was analysed by both stepwise-heating and laser-ablation $^{40}Ar/^{39}Ar$. It shows a staircase stepwise-heating age spectrum with ages ranging from 11 to 70 Ma (Fig. 7a). A Ca/K–Cl/K diagram displaying both stepwise and laser-spot analyses (Fig. 7b) exhibits a cluster at low Ca/K and Cl/K ratios, and mixing trends towards both high Cl/K and Ca/K ratios. In the case of spatially controlled laser-spot data (and by inference also for the stepwise data), the different reservoirs can be identified to represent either melt ("dark") or clast/alteration ("cloudy") phases. Exceptions are most likely the result of gas release from adjacent or underlying melt/clast phases within the fairly inhomogeneous section. Low Ca/K ratios for melt areas obtained from EMPA analyses are in line with this assignment. As seen in the age–Ca/K plot, the corner point representing the pristine melt lies closest to heating steps #5 and 6 and to laser spot #14. It is located at the intersection of alteration and clast-dominated mixing lines (Fig. 7c). Steps 5 and 6 have discordant ages averaging 40 ± 2 Ma, whereas laser spot #14 yields 34 ± 2 Ma (Fig. 7d). EMPA analyses for melt areas have yielded both low and high Cl/K values (up to 0.04) and indicate that Cl is heterogeneously distributed (within the detectability of the EMP) at a scale smaller than the spatial resolution of the electron beam. Recrystallisation phenomena are visible in thin section along the host-rock contacts and are interpreted to be responsible for the rejuvenation visible at low-temperature steps 1–4.

Phyllonitic mylonite PEI27 forms the host rock of pseudotachylyte PEI26 (Fig. 2e). Two adjacent layers from thin, very fine-grained and completely
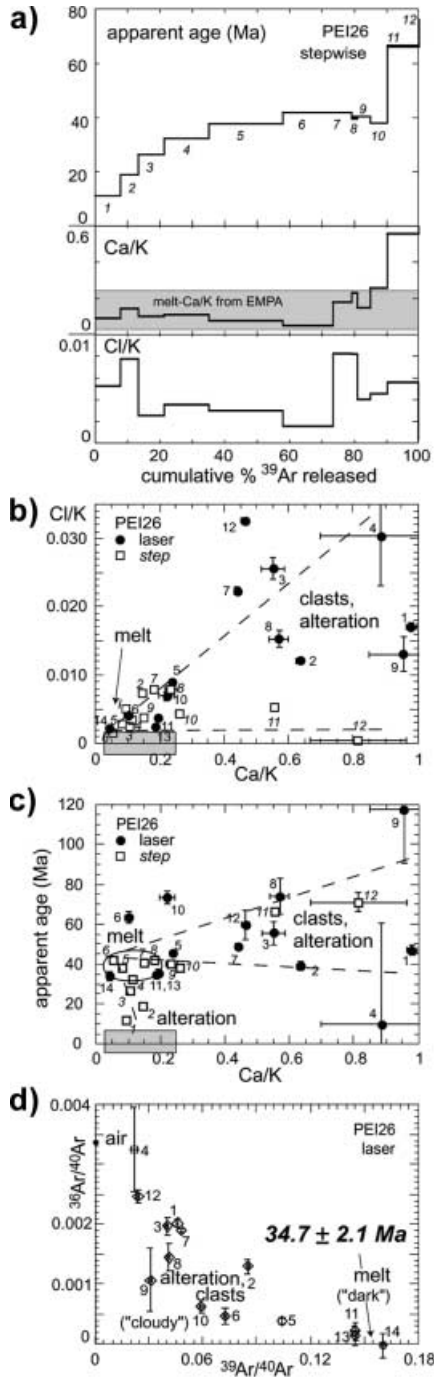
diagrams is identified as due to a mixture between matrix-related material and clast/alteration material. The lowermost Ca/K and Cl/K ratios coincide with EMPA analyses of the melt, whereas higher ratios represent clast/alteration phases. Using the corner-point criterion, step 6 most closely represents the melt, with an age of 37.02 ± 0.04 Ma. If one more conservatively identifies the melt composition as the cluster of four points representing steps 5–8, one obtains a weighted mean age of 36.9 ± 0.6 Ma. EMPA analyses reveal a wider range of Ca/K and Cl/K ratios than that derived from Ar systematics. Both types of analyses have been performed on different pieces of sample (thin sections vs. drill cores) and, in the light of observed inhomogeneities on the mm-scale (cf. Kelley and Spray 1997), no perfect chemical match between the two can be expected.

Fig. 7a–d. Pseudotachylyte PEI26, collected along a shear zone south of the Peio fault. a ⁴⁰Ar/³⁹Ar stepwise-heating spectra, b Cl/K–Ca/K, and c age–Ca/K plots of step-heating and laser-spot analyses. *Shaded areas* denote the range of corresponding, melt-related EMPA analyses. Melt steps and laser spots are located at the intersection of different mixing trends. d Laser-spot isochron plot

laser $^{40}Ar/^{39}Ar$ age of pseudotachylyte PEI26. Because of the small grain size, the mineralogy of the samples analysed could not be determined optically. Based on Rb and Sr concentrations, PEI27/1 is likely to be rich in white mica whereas PEI27/2 contains significant amounts of feldspar. Rb–Sr microsampling analyses of a second mylonite, PEI33, were used to provide additional, independent age control on the pseudotachylyte ages obtained. Six adjacent layers were cut out of adjacent, recrystallised white mica- (PEI33/3, 4, 5, 6) or quartz/feldspar-bearing (PEI33/1, 2) domains from a total area of ~6 mm². Their $^{87}Rb/^{86}Sr$ ratios range between 0.48 and 4.3, and the resulting, poorly defined errorchron indicates an age of 36.8 ± 5.1 Ma (MSWD = 20.3; Fig. 8). The high scatter indicates that Sr isotopic equilibration during mylonitisation was not entirely achieved.

Peio fault

Pseudotachylytes PEI49 and PEI52 and ultramylonite PEI53 were sampled from the same outcrop of the Peio fault. All three samples gave Late Cretaceous ages.

Both stepwise-heating and laser-ablation $^{40}Ar/^{39}Ar$ analyses (25 individual laser spots) were performed on pseudotachylyte PEI49; drill cores for step heating and the slab for laser-spot dating were taken close to the centre of the vein but several mm to cm apart. The stepwise-heating age spectrum shows increasing apparent ages from 50 to ~250 Ma, and a flat middle portion with ages varying between 71 and 78 Ma (~80% ^{39}Ar released; Fig. 9a). Except for the first and last three steps, Ca/K and Cl/K ratios coincide with corresponding values of the pseudotachylyte matrix established using the EMPA raster mode. The Cl/K ratio initially decreases, suggesting the breakdown of a Cl-rich phase during the first steps. By plotting data in a Ca/K–apparent age diagram (Fig. 9b), two divergent mixing trends can be observed. Increasing Ca/K ratios are correlated with slightly increasing apparent (step-heating) ages, pointing towards high-temperature steps 14–16, which is attributed to the degassing of partially resorbed plagioclase clasts inherited from the host rock. A similar trend is indicated by, for example, laser
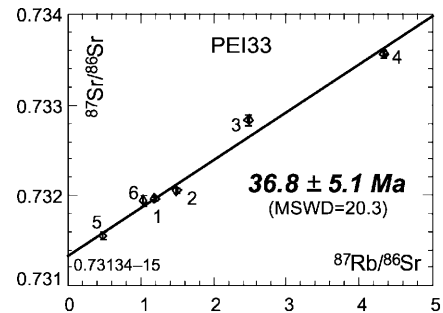
recrystallised ultramylonitic domains were microsampled (PEI27/1 and 2; sample weights 53 and 73 μg). Their different $^{87}Rb/^{86}Sr$ ratios allow the calculation of an age of 35.0 ± 1.1 Ma (Table 4 in electronic supplementary material) which, within error, is similar to the

Fig. 8. Rb–Sr microsampling isochron diagram for orthogneiss mylonite PEI33, collected along a shear zone south of the Peio fault

Fig. 9a–d. Peio fault pseudotachylyte PEI49. **a** $^{40}Ar/^{39}Ar$ stepwise-heating spectra, **b** age–Ca/K, and **c** age–Cl/K plots of both step-heating and laser-ablation analyses. **d** Isochron plot of step-heating and laser-ablation analyses; note that the $^{39}Ar/^{40}Ar$ ratio has been divided by J in order to facilitate comparison between the two techniques (see text for details)
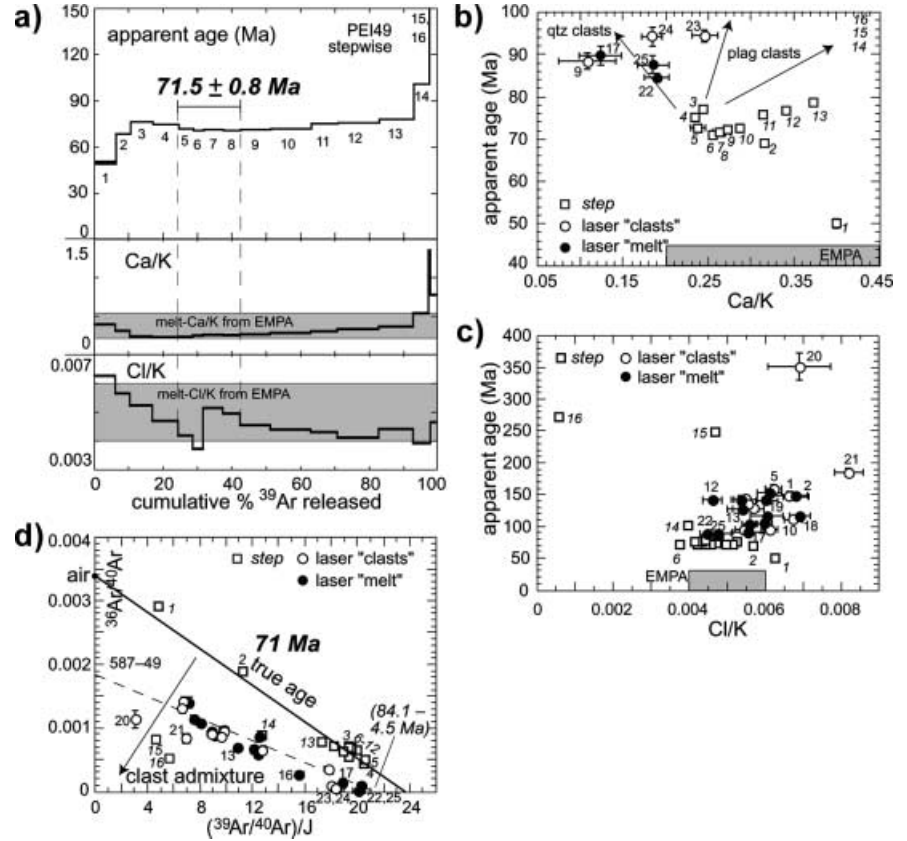
spots #1 and 10. A second trend is revealed by most laser spots and steps 4 and 5, and displays apparent ages negatively correlated with Ca/K; this trend points towards laser spots #20 and 21 (large quartz clasts). Steps 5–8, located at the intersection of these mixing lines, most closely approximate the pristine pseudotachylyte melt and indicate an age of 71.5 ± 0.8 Ma (18% ^{39}Ar released; if steps 3–13 are used, ignoring chemical signatures, the average age still remains in the same range, at 73.8 ± 1.7 Ma). All apparent ages of optically melt-related laser spots (84.6–158.5 Ma) exceed the melt-related stepwise-heating ages. Both Ca/K-age and Cl/K-age correlation plots reveal positive correlations, especially for the laser-ablation analyses (Fig. 9b, c). The laser-spot analyses with the highest Cl/K ratios (higher than any corresponding stepwise data) also record the highest apparent ages, with laser analyses of clasts being one end member (#20, 21). Steps 5–8, representing the pristine pseudotachylyte melt, form the other, low-Cl/K end member. The spatial distribution of old and young laser-spot ages is patchy and changes over distances less than ~1 mm. This demonstrates that varying admixtures of clasts can explain some of the old ages. However, areas which visually appear clast-free (e.g. #2, 18) also show high Ca/K and Cl/K ratios as well as high ages, i.e. they have the typical signature of clasts. Although this could also be explained by some of the trapped/inherited Ar residing in matrix minerals, it is more likely that many of the clasts are smaller than the optical detection

limit of the video camera system. Further support for the latter conjecture comes from the isochron plot (Fig. 9d). In the case of a clearly resolved clast population such as that of JAU 34 (Fig. 4d), clasts plot significantly below and to the left of the isochron defined by matrix points. On the contrary, for PEI49 all optically melt-related laser-spot analyses form a single array (Fig. 9d) which lies to the lower left (without overlap) of the step-heating points which we identified as matrix-related due to their chemical signature. It also lies to the right of clast-related steps (15, 16) and laser spots (#20, 21). This strongly indicates that laser shots did not achieve a clear separation between the two populations. Regressing all analyses except those having large clasts yields an errorchron indicating an age of 84.1 ± 4.5 Ma and a $^{40}Ar/^{36}Ar$ ratio of 587 ± 49. The MSWD of 4.7 indicates scatter outside analytical error due to the presence of small, not fully outgassed clasts. The behaviour of PEI49 is exceptional compared to all other pseudotachylytes we analysed. The differences between both types of $^{40}Ar/^{39}Ar$ results will be discussed in the paragraph on complementarity of techniques (see below). At this stage, we will attribute PEI49 an age of 71–72 Ma.

The discordant stepwise-heating $^{40}Ar/^{39}Ar$ age spectrum of PEI52 yields apparent ages between 29 and >500 Ma, which range between 60 and 70 Ma for ~75% ^{39}Ar released (Fig. 10a). These ages can be evaluated when plotted on a Ca/K–Cl/K diagram, in which all steps form either a tight cluster or two
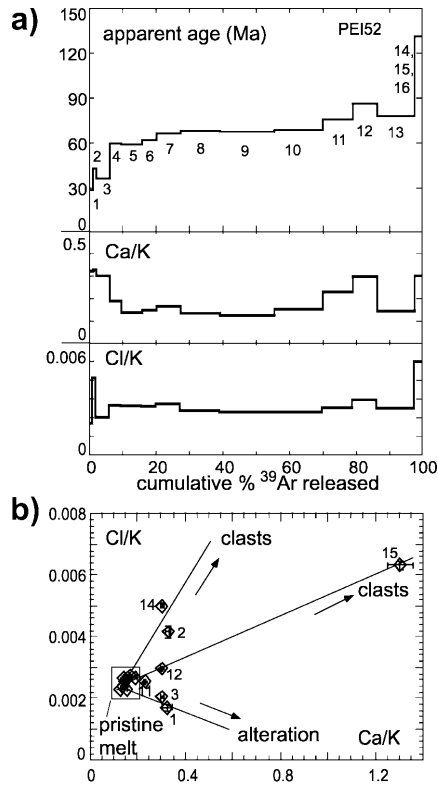
Fig. 10a, b. Peio fault pseudotachylyte PEI52. **a** $^{40}Ar/^{39}Ar$ stepwise-heating spectra, **b** corresponding Cl/K–Ca/K plot based on Ar isotopes

Fig. 11. Rb–Sr microsampling isochron diagram of Peio fault ultramylonite PEI53

divergent mixing trends towards both higher Ca/K and Cl/K ratios (Fig. 10b). The Ca/K-age and Cl/K-age diagrams show similar patterns, and mixing of three chemically and chronologically different phases can be inferred. These include alteration-related minerals characterised by low Cl/K and high Ca/K ratios as well as young ages (steps 1–4), inherited clasts indicated by high Ca/K ratios, high Cl/K ratios and older ages (steps 11–15), and the pseudotachylyte matrix (melt) composition located at the intersection of both mixing trends (steps 5–10). Ages of the latter are interpreted to reflect the pseudotachylyte-forming event, dated at 67 ± 3 Ma. No indication for non-atmospheric, trapped Ar is derived from the isochron plot.

From ultramylonite PEI53, eight adjacent, foliation-parallel layers were prepared using the microdrill (sample weights were between 12 and 125 µg, altogether comprising a square of ∼12 mm^2). These layers have different mineralogical compositions and are devoid of optically resolvable porphyroclasts. Layers 3, 4 and 8 are rich in fine-grained albite and quartz with minor white mica whereas layers 1, 2, 5, 6 and 7 are essentially composed of very fine-grained white mica (Fig. 2c). All eight samples reveal a limited range of $^{87}Rb/^{86}Sr$ ratios of 0.76 to 1.81 and form an errorchron indicating an age of 72.2 ± 9.8 Ma (MSWD = 3.5; Fig. 11). This age is similar, within error limits, to the $^{40}Ar/^{39}Ar$ ages of pseudotachylytes PEI49 and PEI52 from the same
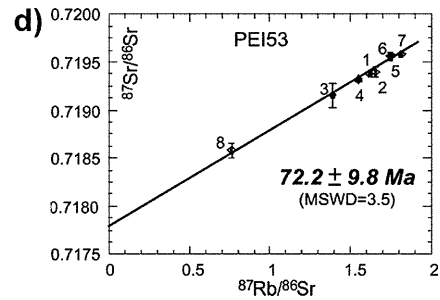
outcrop. It argues for contemporaneous formation of both pseudotachylytes and mylonites during Late Cretaceous times along the Peio fault.

Tonale fault

Pseudotachylyte TO27 was thinner than the microdrill used to core samples for step-heating $^{40}Ar/^{39}Ar$ analysis, and it was therefore analysed by the laser probe only (Fig. 3b). Two profiles across the pseudotachylyte–host rock contact have been analysed, which were precisely located using the BSE image (Fig. 12a). Profile 1 covers a distance of ∼5 mm and comprises nine individual spot analyses, lacking clasts in the case of pseudotachylyte matrix analyses (Fig. 12a, b). Apparent ages within the host rock (spots #10, 11, 9, 5) are 38 Ma at the contact and ∼42 Ma further away. A pronounced peak in apparent ages of 82 Ma is observed within the pseudotachylyte melt at ∼1 mm away from the host-rock contact (spot #3). Ages again decrease to 43 Ma at ∼2.5 mm away from the host-rock contact. A strikingly similar picture is observed for the Cl/K ratio calculated from ^{38}Ar and ^{39}Ar, which also peaks within the first mm of pseudotachylyte. The Ca/K ratio is inversely correlated with both apparent age and Cl/K in the case of profile 1. Profile 2 resembles profile 1, with the exception of a near-monotonous increase of apparent ages within the pseudotachylyte matrix, and both Ca/K and Cl/K ratios being positively correlated with apparent age. The youngest apparent age, 29.3 Ma, is measured for spot #17 located within the host rock, ≤ 0.5 mm away from the contact (profile 2). Taking all analyses together, Cl/K ratios are strikingly positively correlated with apparent ages, with the oldest apparent age (103 Ma) also recording the highest Cl/K ratio (0.0036; profile 2). Plotted on an isochron diagram, all data points scatter around a reference line, which indicates a non-atmospheric, trapped $^{40}Ar/^{36}Ar$ ratio (Fig. 12c). A regression through all pseudotachylyte matrix-related analyses (#2, 3, 4, 6, 7, 8, 12, 13, 16, 18) yields an age of 31.7 ± 8.2 Ma and a $^{40}Ar/^{36}Ar$ ratio of 556 ± 69. If all data points are regressed together, which may be justified considering the apparent resetting of the host rock at the pseudotachylyte contact, a similar age of

Fig. 12a–c. Tonale fault pseudotachylyte TO27. **a** SEM-BSE image showing the locations of the two analysed profiles and other laser spots. **b** Profile 1: laser-ablation ^{40}Ar/^{39}Ar age, Cl/K and Ca/K plots, and **c** corresponding isochron plot
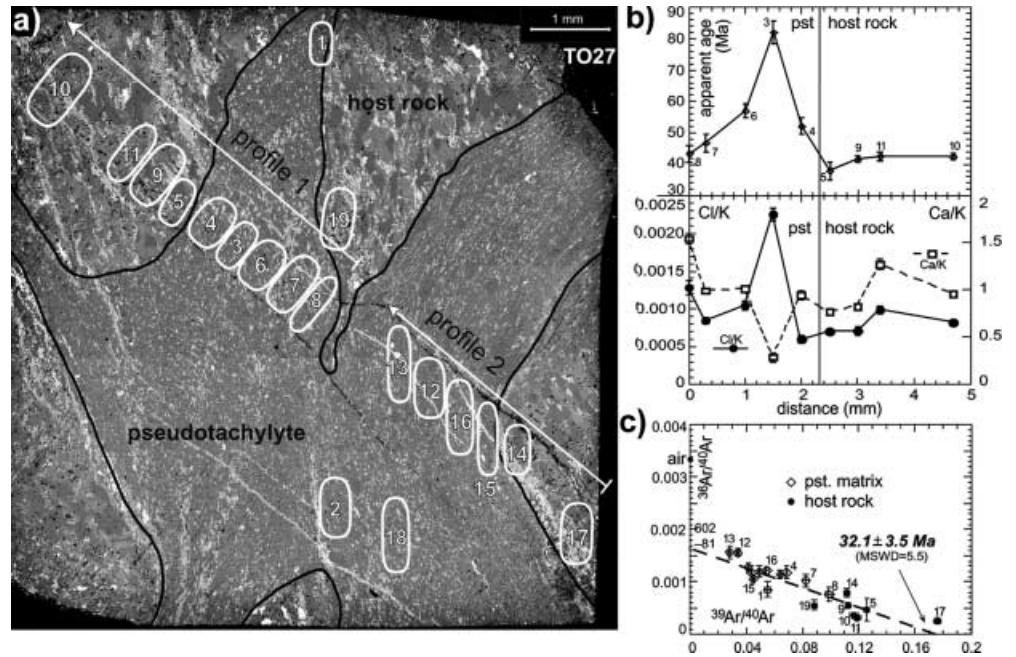
32.1 ± 3.5 Ma and trapped ^{40}Ar/^{36}Ar value of 602 ± 81 are indicated. On the other hand, Kelley et al. (1994) have demonstrated that pseudotachylyte formation is ineffective in resetting ages in the host rock, even on the mm-scale. Biotite Rb/Sr and K/Ar ages from a wide area of the hosting Tonale unit are essentially older than 100 Ma (Thöni 1981; Del Moro, unpublished data) and record very weak Alpine (< 90 Ma) metamorphic overprint, which contrasts the young host-rock ages at the contact to the pseudotachylyte TO27. Local, fluid(?)-induced resetting in the immediate vicinity of the fault may be a feasible resetting mechanism for the host rock. However, lacking detailed geochronological data from the host rock of TO27, no definitive conclusion can be drawn here. The ~32 Ma age is corroborated by a pseudotachylyte age reported from the adjacent North Adamello area south of the Tonale fault, with a well-defined age of 29–30 Ma (Pennacchioni and Villa, unpublished data). Considering an uncertainty of 8 Ma for the "pseudotachylyte only" spots, a younger age of ~25 Ma for TO27 cannot be entirely ruled out.

Discussion and interpretation

Suitability of pseudotachylytes for ^{40}Ar/^{39}Ar dating

Because of potassium concentrations lying between those for amphiboles and micas (mean of $3.7 \pm 1.7\%$, $n = 20$, variation between 0.8 and 9.5%; see also Müller et al. 2001), pseudotachylytes are well-suited and increasingly utilised targets for ^{40}Ar/^{39}Ar dating (Reimold et al. 1990, 1992; Trieloff et al. 1994; Kelley et al. 1994; Spray et al. 1995; Kelley and Spray 1997; Magloughlin et al. 2001; Sherlock and Hetzel 2001). Significant variation in K concentration can exist within the same

sample (PAL35B; Müller 1998), where the injection vein shows a potassium concentration almost twice as high as the level documented in the adjacent fault vein (3.2 vs. 1.7%). Since injection veins also contain fewer inherited clasts, they are generally better suited for dating than fault veins. The high Ca and Cl concentrations of pseudotachylytes make them ideal materials to fully exploit phase discriminations based on element correlation systematics.

Stepwise-heating ^{40}Ar/^{39}Ar analysis of pseudotachylytes

The chemical information provided by reactor-produced ^{37}Ar (Ca), ^{38}Ar (Cl) and ^{39}Ar (K) together with EMPA analyses of the pseudotachylyte matrix and clasts is an important key to the interpretation of resultant ^{40}Ar/^{39}Ar ages. Chemically distinct mineral phases which release Ar at different stages during the step-heating experiment can be identified using Ca/K and Cl/K spectra, which has been used for the interpretation of the resulting age spectra. It allows a qualitative discrimination of mineral phases constituting the pseudotachylyte. Petrographic observations from these samples demonstrate that clasts, alteration phases and magmatic minerals all coexist next to each other. Alteration phases are often characterised by elevated Cl/K ratios and release argon at low temperatures. Inherited clasts comprise plagioclase with high Ca/K ratios and/or fluid-inclusion-bearing quartz with elevated Cl/K ratios. The determination of matrix-related Ca/K and Cl/K ratios using microprobe analyses (raster mode) is a prerequisite to identifying those steps during which Ar is released from matrix minerals (e.g. PEI12, PEI49; Figs. 6, 9). For the samples presented here, Ca/K and Cl/K ratios

frequently show divergent mixing trends towards alteration and clast phases, with the pristine matrix/melt composition being located at the intersection of those trends (e.g. Figs. 4, 6, 9, 10). In order to evaluate the significance of apparent ages, the results of stepwise-heating analyses must be checked for the presence of non-atmospheric, trapped Ar compositions using isochron plots on isochemical steps. Most stepwise-heating analyses, however, show no evidence of non-atmospheric, trapped Ar components (PEI49, PEI12, JAU10, JAU34A), and thus the resulting apparent ages are interpreted to be geologically significant.

Considering the small grain sizes ($> 1–3$ μm) of some of the newly crystallised pseudotachylyte matrix minerals (e.g. biotite), recoil of the reactor-produced Ar isotopes ^{37}Ar and ^{39}Ar may cause effects to be seen in the ^{40}Ar/^{39}Ar analyses. ^{39}Ar$_K$ and ^{37}Ar$_{Ca}$ have mean recoil distances of ∼80 and ∼300 nm respectively, whereas ^{38}Ar$_{Cl}$ recoils only negligibly (< 1 nm; Onstott et al. 1995; Villa 1997). The overall pattern of most stepwise-heating age spectra presented, namely, young ages at low temperatures and old ages at highest temperatures, could in principle be explained by recoil ^{39}Ar loss out of a mineral finally degassing at highest temperatures. If recoil of ^{39}Ar caused the old ages at highest temperatures, then the corresponding Ca/K ratios would concomitantly decrease because ^{37}Ar shows an approximately fourfold recoil distance. All age spectra, however, record increasing Ca/K ratios at highest temperatures which rule out significant recoil loss and/or redistribution. This supports the interpretation that inherited old plagioclase porphyroclasts degas at highest experimental temperatures. Magloughlin et al. (2001) investigated ^{39}Ar recoil in pseudotachylyte by vacuum encapsulation and found low recoil losses between 0.2 to 8.4%. Trieloff et al. (1994) reported a ^{39}Ar recoil redistribution in their pseudotachylyte samples of at most 1.6%. In our case, the similarity of ages of kinematically similar mylonites and pseudotachylytes, and the internal consistency of ages between step-heating and laser-ablation ^{40}Ar/^{39}Ar analyses support the interpretation that no significant recoil loss of ^{39}Ar occurred within the pseudotachylytes investigated.

In order to assess whether the old apparent ages recorded at highest temperatures of stepwise-heating experiments are geologically meaningful, these ages are compared with corresponding ages of laser-spot analyses of big clasts (feldspar or quartz) and ages of the country rocks. Two laser-spot ages of big clasts from PEI49 are 185 and 351 Ma, whereas highest-temperature steps of the corresponding age spectrum record ages of 249 and 272 Ma. Laser-spot ages of clasts from pseudotachylyte JAU34A range between 111 and 434 Ma and compare with the 500 Ma recorded at highest temperatures during the stepwise-heating experiment. In both samples, the range of ages observed for both laser-spot analyses of clasts and highest-temperature steps precludes any accurate derivation of ages of the precursor rock. It appears that even clasts larger than > 500 μm are at least partially reset. However, the oldest ages for both pseudotachylytes compare favourably with typical Variscan (∼330 Ma) and/or Caledonian ages (∼450 Ma) which have been described in the western Austroalpine unit (e.g. Hoinkes and Thöni 1993; Spiess 1995).

Laser-melting ^{40}Ar/^{39}Ar analysis of pseudotachylytes

The striking advantage of the laser probe is its spatial resolution, which in many cases allowed discrimination between Ar residing within matrix minerals and clasts. This is best illustrated by sample JAU34A which shows two well-resolved clusters of spot analyses belonging to either clasts or matrix (Fig. 4d). A similar, tight cluster of matrix-related laser-spot analyses was measured for pseudotachylyte RU23 (Müller et al. 2001). No indication for non-atmospheric, trapped argon is found for JAU34A. The age difference between JAU10 (16.5 ± 0.8 Ma) and JAU34 (19.7 ± 0.5 Ma) reflects fault activity lasting for a few million years (cf. Müller et al. 2000b). The spatial resolution of the laser probe could also be successfully utilised for partially recrystallised pseudotachylytes (e.g. PEI26; Fig. 7). In the case of PEI26, some laser-spot analyses of the dark matrix chemically resembled melt-related steps 5–8 and yielded an age concordant with cogenetic fault rocks (mylonites PEI27, PEI33).

The most interesting results with respect to Ar systematics in pseudotachylytes were obtained from samples PEI49 and TO27. When plotted on isochron diagrams, both revealed the presence of elevated amounts of non-atmospheric, trapped Ar (Figs. 9d, 12c). In these cases, the chemical information provided by the laser-spot Cl/K and Ca/K ratios and the textural information from BSE images (clast, matrix or host rock) was crucial for a reliable interpretation. Pseudotachylyte PEI49 showed a positive trend between chemical indicators (Cl/K, Ca/K ratios) and apparent age (i.e. ^{40}Ar). The highest age derives from clasts having the highest Ca/K and Cl/K ratios (Fig. 9c). We therefore propose that not only Ca-rich plagioclase but also quartz with high ^{40}Ar/^{36}Ar ratios (Cumbest et al. 1994) and high Cl concentrations in fluid inclusions derived from Cl-rich brines (McCaig 1997) are responsible for this positive correlation. The Ca/K and Cl/K ratios may thus be used to monitor the presence of inherited ^{40}Ar (Villa 1991; Esser et al. 1997). It appears to be possible that Cl-rich fluid inclusions shielded in quartz porphyroclasts may survive an extremely short-lived, pseudotachylyte-forming event with temperatures above their decrepitation temperature (< 600 °C, Villa 2001). Because of the abundance of small clasts within PEI49, incompletely re-equilibrated quartz and plagioclase clasts retaining old Ar and high-Cl signatures are interpreted to be one source for the old apparent ages. However, visually clast-free analyses irregularly distributed within the matrix also show old ages associated to high Cl/K ratios. This may be the result of both (1) a clast size distribution in sample

PEI49 which could not be fully assessed by optical examination using the laser-probe camera and/or (2) high $^{40}Ar/^{36}Ar$ signatures liberated locally from degassed old clasts during short-lived frictional melting, and which were subsequently (partly) retained by crystallising matrix minerals. In principle, it would be desirable to achieve a distinction between inherited Ar and excess Ar. *Inherited* Ar is unequilibrated Ar located in mineral relics. Each individual clast underwent a different partial resetting and no correlation of ^{40}Ar with ^{36}Ar is expected (indeed, none was found, e.g. in sample JAU34; Fig. 4d). *Excess* Ar is generally assumed to be externally derived from fluids (Cumbest et al. 1994) and should therefore be isotopically equilibrated. In the case of PEI49, laser extractions define an isochron, regardless of the chemical signature of the regressed points (Fig. 9d). Taken at face value, this would require a simple binary mixing between one radiogenic end member with an age of 84 Ma and a well-homogenised, trapped Ar, common both to "matrix" and "clast" laser spots, implying that clasts and matrix were in isotopic equilibrium. This interpretation poses two paradoxes, since the age conflicts with the step-heating results, and the equilibration of the clasts with the matrix conflicts with the presence of unequilibrated clasts in all other samples. We therefore use the term *inherited* Ar to denote any ^{40}Ar component unsupported by decay of ^{40}K after formation of the respective samples.

From sample TO27, two laser-spot age traverses across the pseudotachylyte–host rock boundary revealed the oldest apparent ages within the pseudotachylyte matrix ∼1 mm away from the contact, and surprisingly young apparent ages within the host rock ≤ 0.5 mm away from the contact (Fig. 12). Old apparent ages within the pseudotachylyte adjacent to the host rock are interpreted to reflect localised high concentrations of ^{40}Ar released from the host rock during frictional melting. These gradients in Cl, Ca and inherited ^{40}Ar appear to resemble a reaction front which was immediately frozen in by the crystallising matrix minerals, as revealed by interlocking "magmatic" textures. The chemical indicators (mainly Cl/K, partly Ca/K) and apparent age again correlate positively (without visually noticeable clasts), supporting the interpretation that they can be used as an indicator of inherited ^{40}Ar components (Fig. 12b).

Effects of alteration of the pristine pseudotachylyte are mainly seen in low-temperature increments of stepwise-heating experiments, as indicated by anticorrelated age vs. Cl/K ratio relationships. Although carefully selected, the effects of cracks or joints bearing, e.g. brownish, secondary Fe-hydroxides or clays cannot be excluded for at least some of the mg-sized samples used for stepwise-heating analyses. On the contrary, the locations of individual laser-spot analyses were carefully chosen on the basis of observations using reflected light and BSE images, which reduces the chance of hitting strongly altered parts or at least helps with their identification. However, weakly negatively correlated apparent ages and Cl/K ratios of laser-spot analyses of RU23 indicate that alteration may also be present in carefully chosen laser-spot analyses (Müller et al. 2001).

Complementarity of $^{40}Ar/^{39}Ar$ techniques

In our young (Tertiary–Cretaceous) samples, sample size requirements were such that the spatial resolution of the laser microprobe was limited to 0.5 mm^2 (e.g. ∼700×700 μm), but theoretically it is below 100 μm. In most cases, this was sufficient to identify different areas of the sample in their microstructural context. On the other hand, step-heating exploits a different mechanism of Ar release, namely, sequential in-vacuo breakdown. Villa et al. (2000) have argued that they were able to discriminate Ar deriving from < 20 μm amphibole relics based on the Ca–Cl–K correlations. The present study has successfully identified 100-μm-sized clasts as carriers of inherited Ar by laser microprobe dating, and in so doing has attributed a distinctive Ca–Cl–K signature to the clasts and a different one to the matrix. The identification of clasts at even smaller length scale is straightforward basing on their Ca–Cl–K signature in the course of a step-heating analysis, as it is seen that this signature is associated to delayed breakdown at furnace temperatures > ∼1,200 °C. This parallel approach to clast–matrix discrimination allows to fully exploit the potential of step heating to selectively break down minerals. In principle, it would seem possible to be able to discriminate between mineral phases which are intergrown or mixed at scales < < 100 μm. In practice, it must be kept in mind that ^{39}Ar and ^{37}Ar undergo irradiation recoil of 0.1 and 0.3 μm respectively (Onstott et al. 1995), and any Ar reservoir < 0.5 μm is smeared out by recoil.

The different scales and Ar release mechanisms of both laser-spot and stepwise-heating $^{40}Ar/^{39}Ar$ dating affect the K–Ar clock in different ways. The results of the two experimental approaches for two samples converge (JAU34A, PEI26), whereas in the case of PEI49 they do not provide concordant ages. In the former cases, the resulting age estimates are internally but also externally strengthened by comparison to other cogenetic pseudotachylytes or mylonites. The unusual behaviour of PEI49 is best revealed by the laser-spot analyses plotting below the isochron defined by the step-heating data which points towards atmospheric, trapped $^{40}Ar/^{36}Ar$. In order to reconcile these observations, it is necessary to note that the individual laser spots are characterised mainly by higher Cl/K (and partly also Ca/K) ratios when compared to the step-heating data (Fig. 9b, c). We argue that the laser spots essentially always (albeit in varying proportions) sampled both melt and optically unresolvable clasts, and the resultant ages are therefore offset to higher Cl/K ratios, with the Cl residing also in fluid inclusions in quartz. The presence of high amounts of non-atmospheric, trapped Ar appears to be a local and rare phenomenon only, as hinted by the very patchy distribution of high trapped-^{40}Ar

locations which are averaged out for the $\sim$100 mg sample used for the stepwise-heating analysis. As a result, the laser analyses of PEI49 yield no accurate age information. However, they can readily be reconciled with the Upper Cretaceous age (71–72 Ma) provided by the step-heating analyses, if one takes into account the different scale at which the two complementary methods operate (see above).

Rb–Sr microsampling vs. K–Ar dating of pseudotachylytes

Although sampled on the mm^2-scale of a thick section, Rb–Sr analyses of the two samples investigated (PEI12, JAU10) did not yield chronological information. Although sample JAU10 revealed remarkable differences with respect to Rb–Sr ratios, the severe scatter of data points even on the mm-scale precluded the derivation of reliable chronological information. It seems that incomplete resorption of plagioclase during frictional melting prevents the liquid pseudotachylyte melt from equilibrating with respect to Rb–Sr over distances of several mm to cm before solidification. In addition, JAU10 also shows incipient alteration.

The lack of Rb–Sr isotopic homogenisation on the 10–15 mm scale contrasts with the resetting of the K–Ar chronological system for $\sim$100 mg (matrix) samples. Different resetting mechanisms appear to be operating for the two chronometers. Sr isotopic homogenisation in rhyolitic melts by diffusion is $\sim$1–2 orders of magnitude slower than Ar diffusion in similar melts (see Perez and Dunn 1996; Behrens and Zhang 2001), although in detail this difference depends on composition, water content, pressure, temperature, etc. However, when considering the short time scales during which pseudotachylytes are formed, diffusional equilibration may be relatively unimportant. Instead, segregation of a vapour phase during melt generation will accumulate most Ar released during frictional melting because of the extreme incompatibility of Ar (e.g. Brooker et al. 1998). This mechanism may be responsible for the complete K–Ar resetting of most samples. Ar gradients appear also to be frozen into the newly formed melt (e.g. TO27), possibly related to fast quenching.

Formation vs. cooling ages

Reimold et al. (1990) extrapolated diffusion parameters for their Vredefort pseudotachylytes from stepwise-heating experiments, and proposed that Ar is nearly quantitatively lost for a pseudotachylyte kept at 250 °C for $\sim$10 Ma. However, pseudotachylytes are partially composed of hydrous minerals such as biotite which structurally decompose during stepwise-heating at temperatures > 600 °C (Lo et al. 2000). Deducing diffusion parameters from such experiments is likely to yield misleading results for the Ar resetting behaviour of pseudotachylytes.

The presence of matrix phases with slight but significant chemical and chronological heterogeneities, and clasts in mutual isotopic disequilibrium implies that diffusive homogenisation played a negligible role. The "closure age" concept is not applicable in cases where mineral zones retain their distinct chemical and isotopic signature. The coexistence of several diachronic mineral generations allows at most one of them (the oldest one) to be a "cooling age", whereas all younger heterochemical zones necessarily correspond to formation ages. In this context, it is essential to bear in mind that staircase-shaped $^{40}Ar/^{39}Ar$ step-heating spectra do not reflect any sort of "diffusive gradients" (e.g. Hodges et al. 1994; Villa et al. 1997); on the contrary, to the extent that staircases can be correlated with Ca/K and/or Cl/K, they represent heterochemical mineral zones precisely lacking diffusive re-equilibration.

In addition to this argument, there is empirical support for the interpretation that the presented pseudotachylyte ages are formation ages. In two cases, $^{40}Ar/^{39}Ar$ analyses of pseudotachylytes have been compared with ages of cogenetic mylonites obtained by Rb–Sr microsampling of thin, fully dynamically recrystallised layers. Peio fault-related ultramylonite PEI53 yielded a rather imprecise age of 72.2 ± 9.8 Ma because of limited spread in the Rb/Sr ratios. It compares well with the stepwise-heating ages of pseudotachylytes PEI49 and PEI52 (71.5 ± 0.8 Ma and 67 ± 3 Ma respectively) collected from the same outcrop. The laser-ablation isochron age of > 80 Ma for PEI49 is likely to be affected by the ubiquitous presence of submicroscopic clasts, as discussed above. In one outcrop along shear zones south of the Peio fault, phyllonitic ultramylonite (PEI27) forms the host rock of pseudotachylyte (PEI26). Both yielded indistinguishable ages of 35.0 ± 1.1 Ma (PEI27) and 34.7 ± 2.1 Ma (PEI26, laser). Samples from other locations along these shear zones yielded ages of 36.9 ± 0.6 Ma (pseudotachylyte PEI12) and 36.8 ± 5.1 Ma (mylonite PEI33). The clustering of ages between 35 and 37 Ma argues both for contemporaneity of mylonites and pseudotachylytes and for the reliability of the $^{40}Ar/^{39}Ar$ pseudotachylyte ages obtained. These mylonites were formed at low syndeformational temperatures in the range of 250 to 300 °C, for which the Rb–Sr isotopic system of fine-grained white mica records formation ages. By inference, the similar ages of cogenetic pseudotachylyte are also interpreted to represent formation ages.

Relationship between pseudotachylyte ages and tectonics

The ages of the pseudotachylytes collected along different faults range from 72 to 17 Ma but they are self-consistent among the individual faults. A detailed assessment of their tectonic implications can be found in Müller et al. (2001) and only a brief summary is given

here. The Miocene ages established for Jaufen fault pseudotachylytes (JAU10, 34A) coincide with overall Neogene extension of the Alps. This is independently dated by Early–Middle Miocene sedimentary basins (~17 Ma; Karpatian) bound to extension-related faults (Ratschbacher et al. 1991; Decker and Peresson 1996) and the contemporaneous exhumation of the Lepontine dome and the Tauern window (e.g. Von Blanckenburg et al. 1989; Grasemann and Mancktelow 1993). An Oligocene age of TO27 agrees well with the deformation of the Periadriatic plutons (32–30 Ma). Late(st) Eocene fault ages (PEI12, 26, 27, 33) represent a so-far undocumented top-to-(W)NW thrusting event immediately south of the Peio fault, whereas Late(st) Cretaceous ages along the Peio normal fault (PEI49, 52, 53) coincide with a period of enhanced normal faulting (Fügenschuh et al. 2000) and Late Cretaceous–Palaeocene sedimentation (Gosau group; Wagreich and Faupl 1994), and are in line with the Peio fault being cut by an Oligocene dyke (Müller et al. 2001).

Conclusions

The integration of chemical and chronological information provided by electron microprobe, SEM and geochronological methods enables accurate dating of pseudotachylytes if the results are carefully and individually assessed. However, the small grain size of newly grown matrix minerals, the presence of both inherited clasts and secondary alteration phases, and the existence of inherited argon components cause difficulties for geochronological investigations of pseudotachylytes.

1. Age spectra of ^{40}Ar/^{39}Ar stepwise-heating analyses of pseudotachylytes have to be interpreted together with chemical information from reactor-produced Ar isotopes from K, Ca and Cl, and independent chemical data provided by EMPA and/or SEM. This approach allows identification of steps related to the pseudotachylyte melt and thus pseudotachylyte formation. Complex stepwise-heating age spectra result from two competing effects: preservation of undegassed clasts and recrystallisation/alteration of the pseudotachylyte matrix.
2. Pseudotachylytes (locally) contain significant amounts of inherited ^{40}Ar, derived from incomplete degassing of precursor minerals which is facilitated by the short time scale of frictional melting. Apparent ages should be considered with caution and should be evaluated using isochron plots limiting to steps/laser spots having the Ca–Cl–K signature of the matrix consistent with EMPA data. Cl/K ratios may be raised or lowered as an effect of alteration, depending on the chemistry the secondary fluid relative to the unaltered material. In either case, Cl/K ratios are useful to identify extraneous minerals, potential carriers of inherited ^{40}Ar, especially when used in connection with the Ca/K ratio.

3. The spatial resolution of laser-ablation ^{40}Ar/^{39}Ar analyses is in most cases sufficient to discriminate between newly formed melt and surviving clasts. However, it fails in the case of very fine-grained clasts (PEI49). In this case, old apparent ages are often associated with high Cl/K ratios and thus readily identified as due to clast contamination. Laser analyses further allow to ascertain the Cl–Ca–K signature of clasts, validating the inferences of step-heating analyses.
4. The complementary use of laser analyses (which spatially allow to identify Ar reservoir minerals) and step-heating analyses (which exploit the differential thermal breakdown of these reservoirs) allows to greatly increase the spatial resolution of the ^{40}Ar/^{39}Ar method. As an example, clasts do not need to be visible under a microscope in order to be identified by their Ca–Cl–K signature; the limit of our approach is the recoil distance of ^{37}Ar and ^{39}Ar.
5. Rb–Sr microsampling dating of pseudotachylyte does not yield reliable chronological information which can be related to pseudotachylyte-forming events. This results from incomplete Sr equilibration because plagioclase is often a restite in the pseudotachylyte melt.
6. Concordant ages between cogenetic mylonites and pseudotachylytes, as well as the preservation of isotope disequilibria within pseudotachylytes indicate that pseudotachylyte ^{40}Ar/^{39}Ar ages date the frictional melting process itself and are not perturbed by subsequent open-system behaviour.

Appendix

Sample locations

The co-ordinates (right, down) refer to the sheets given in brackets of the Italian (and Austrian) national maps, scale 1:50.000.

JAU10

pseudotachylyte: SE ridge of small creek, 250 m east of Leitebenalm, between first and second bend of Jaufenpass/Pso. di M. Giovo road in direction St. Leonhard in Passeier (S. Leonardo in Passiria, Italy), alt. 1,900 m; co-ordinates 224900, 189000 (Austrian map #174, Timmelsjoch).

JAU34A

pseudotachylyte: same locality as JAU10 but loose block, ∼100 m away from JAU10.

PEI12

pseudotachylyte: loose block (with Tonale unit affinity) collected at Forcellina di Montozzo, alt. 2,613 m, 7 km north-east of Ponte di Legno (Val di Sole, Italy); co-ordinates 621350, 5129500 (#41, Ponte di Legno).

PEI26

pseudotachylyte, PEI27 – ultramylonite/phyllonite: 100 m south of Passo Cercena, 1 m west of crest, alt. 2,632 m, 4.5 km east-north-east of Pejo (Italy); co-ordinates 632750, 5138100 (#42, Malè).

PEI33

mylonite: road cut along forest road in Val Comasine, west side of Valle di Pejo (Italy), ∼400 m south of Malga Val Comasine, alt. ∼2,050 m; co-ordinates 628400, 5132800 (#042, Malè).

PEI49

pseudotachylyte: eastern crest of Cocchiole, alt. ∼2,620 m, ∼250 m east of main peak, small "valley" with military tunnels (WWI Italy), 3 m above highest military tunnel; 8 km (west)south-west of Pejo (Italy); co-ordinates 622750, 5130850 (#041, Ponte di Legno).

PEI52

pseudotachylyte: same as PEI49, alt. ∼2,617 m, 0.5 m above highest military tunnel.

PEI53

ultramylonite: same as PEI49, alt. ∼2,615 m, at the level of the highest military tunnel.

TO27

pseudotachylyte: outcrop (excavation site) in Pellizzano, direction Cusiano, Val di Sole (Italy); co-ordinates 635300, 5130350 (#42, Malè).

References

Andriessen PAM, Boelrijk NAIM, Hebeda EH, Priem HNA, Verdurmen EAT, Verschure RH (1979) Dating the events of metamorphism and granitic magmatism in the Alpine Orogen of Naxos (Cyclades, Greece). Contrib Mineral Petrol 69:215–225

Austrheim H, Boundy TM (1994) Pseudotachylytes generated during seismic faulting and eclogitization of the deep crust. Science 265:82–83

Behrens H, Zhang Y (2001) Ar diffusion in hydrous silicic melts: implications for volatile diffusion mechanisms and fractionation. Earth Planet Sci Lett 192:363–376

Bigi G, Cosentino D, Parotto M, Sartori R, Scandone P (1990) Structural model of Italy, sheets 1 and 2. CNR Italy

Brooker RA, Wartho J-A, Carroll MR, Kelley SP, Draper DS (1998) Preliminary UVLAMP determinations of argon partition coefficients for olivine and clinopyroxene grown from silicate melts. Chem Geol 147:185–200

Cumbest RJ, Johnson EL, Onstott TC (1994) Argon composition of metamorphic fluids: implications for $^{40}Ar/^{39}Ar$ geochronology. Geol Soc Am Bull 116:942–951

Decker K, Peresson H (1996) Tertiary kinematics in the Alpine-Carpathian-Pannonian system: links between thrusting, transform faulting and crustal extension. In: Wessely G, Liebl W (eds) Oil and gas in alpidic thrustbelts and basins of Central and Eastern Europe. EAGE Spec Publ 5:69–77

Del Moro A, Sassi F, Zirpoli G (1982) New radiometric data on the Alpine thermal history in the Ötztal-Merano area (Eastern Alps). Mem Sci Geol 35:319–325

Esser RP, McIntosh WC, Heizler MT, Kyle PR (1997) Excess argon in melt inclusions in zero-age anorthoclase feldspar from Mt. Erebus, Antarctica, as revealed by the $^{40}Ar/^{39}Ar$ method. Geochim Cosmochim Acta 61:3789–3801

Froitzheim N, Conti P, van Daalen M (1997) Late Cretaceous, synorogenic, low-angle normal faulting along the Schlinig fault (Switzerland, Italy, Austria) and its significance for the tectonics of the Eastern Alps. Tectonophysics 280:267–293

Fügenschuh B, Mancktelow NS, Seward D (2000) Cretaceous to Neogene cooling and exhumation history of the Oetztal-Stubai basement complex, eastern Alps: A structural and fission track study. Tectonics 19:905–918

Giletti BJ, Casserly, JED (1994) Strontium diffusion kinetics in plagioclase feldspars. Geochim Cosmochim Acta 58:3785–3793

Glutz C (1997) Kinematik der Jaufenlinie. Diploma Thesis, ETH Zürich, p 102

Grasemann B, Mancktelow NS (1993) Two-dimensional thermal modelling of normal faulting: the Simplon Fault Zone, Central Alps, Switzerland. Tectonophysics 225:155–165

Hammouda T, Pichavant M, Chaussidon M (1996) Isotopic equilibration during partial melting: an experimental test of the behaviour of Sr. Earth Planet Sci Lett 144:109–121

Hodges KV, Hames WE, Bowring SA (1994) Ar-40/Ar-39 age gradients in micas from a high-temperature low-pressure metamorphic terrain – evidence for very slow cooling and implications for the interpretation of age spectra. Geology 22:55–58

Hoinkes G, Thöni M (1993) Evolution of the Ötztal-Stubai, Scarl-Campo and Ulten Basement Units. In: von Raumer JF, Neubauer F (eds) Pre-Mesozoic geology in the Alps. Springer, Berlin Heidelberg New York, pp 485–494

Kelley SP, Spray JG (1997) A late Triassic age for the Rochechouart impact structure, France. Meteor Planet Sci 32:629–636

Kelley SP, Reddy SM, Maddock R (1994) Laser-probe ^{40}Ar-^{39}Ar investigations of a pseudotachylyte and its host rock from the Outer Isles thrust, Scotland. Geology 22:443–446

Kronenberg AK, Segall P, Wolf GH (1990) Hydrolytic weakening and penetrative deformation within a natural shear zone. In: Duba AG et al. (eds) The brittle-ductile transition in rocks (The Heard Volume). Geophys Monogr 56:21–36

Lo C-H, Lee JKW, Onstott TC (2000) Argon release mechanisms of biotite in vacuo and the role of short-circuit diffusion and recoil. Chem Geol 165:135–166

Magloughlin JF, Spray JG (1992) Frictional melting processes and products in geological materials: introduction and discussion. In: Magloughlin JF, Spray JG (eds) Frictional melting processes and products in geological materials. Tectonophysics 204:197–204

Magloughlin JF, Hall CM, van der Pluijm BA (2001) ^{40}Ar-^{39}Ar geochronometry of pseudotachylytes by vacuum encapsulation: North Cascade Mountains, Washington, USA. Geology 29:51–54

Martin S, Prosser G, Santini L (1991) Alpine deformation along the Periadriatic lineament in the Italian Eastern Alps. Ann Tect 5:118–140

Martini JEJ (1991) The nature, distribution and genesis of the coesite and stishovite associated with pseudotachylite of the Vredefort Dome, South Africa. Earth Planet Sci Lett 103:285–300

McCaig A (1997) The geochemistry of volatile fluid flow in shear zones. In: Holness MB (ed) Deformation-enhanced fluid

transport in the Earth's crust and mantle. Mineral Soc Ser 8:227–266

McDougall I, Roksandic Z (1974) Total fusion ^{40}Ar/^{39}Ar ages using HIFAR reactor. J Geol Soc Aust 21:81–89

Müller W (1998) Isotopic dating of deformation using microsampling techniques: the evolution of the Periadriatic Fault System (Alps). PhD Thesis, ETH Zürich no 12580, p 135

Müller W, Mancktelow NS, Meier M (2000a) Rb-Sr microchrons of synkinematic mica in mylonites. Earth Planet Sci Lett 180:385–397

Müller W, Aerden D, Halliday AN (2000b) Isotopic dating of strain fringe increments: Duration and rates of deformation in shear zones. Science 288:2195–2198

Müller W, Prosser G, Mancktelow NS, Villa IM, Kelley SP, Viola G, Oberli F (2001) Geochronological constraints on the evolution of the Periadriatic Fault System (Alps). Int J Earth Sci (Geol Rundsch) 90:623–653

Onstott TC, Miller ML, Ewing RC, Arnold GW, Walsh DS (1995) Recoil refinements: Implications for the ^{40}Ar/^{39}Ar dating technique. Geochim Cosmochim Acta 59:1821–1834

Parolini F (1997) Kinematik der Jaufenlinie. Diploma Thesis, ETH Zürich, p 105

Perez WA, Dunn T (1996) Diffusivity of strontium, neodymium, and lead in natural rhyolite melt at 1.0 GPa. Geochim Cosmochim Acta 60:1387–1397

Petermann ZE, Day W (1989) Early Proterozoic activity on Archean faults in the western Superior province. Evidence from pseudotachylite. Geology 17:1089–1092

Pouchon JL, Pichoir F (1984) Un nouveau modèle de calcul pour la microanalyse quantitative par spectrometrie de rayons X. I. Application à l'analyse d'échantillons homogènes. Rech Aerospat 184:167–192

Ratschbacher L, Frisch W, Linzer HG, Merle O (1991) Lateral extrusion in the Eastern Alps, part 2. Structural analysis. Tectonics 10:257–271

Reimold WU, Oskierski W (1987) The Rb-Sr-age of the Rochechouart impact structure, France, and geochemical constraints on melt-target rock-meteorite compositions. In: Pohl J (ed) Research in terrestrial impact structures. Earth Evolution Science Series. Vieweg, Wiesbaden, pp 94–114

Reimold WU, Jessberger EK, Stephan T (1990) ^{40}Ar-^{39}Ar dating of pseudotachylite from the Vredefort dome, South Africa: a progress report. Tectonophysics 171:139–152

Reimold WU, Stephan T, Jessberger EK (1992) Testing younger than 2 Ga ^{40}Ar–^{39}Ar ages for pseudotachylite from the Vredefort structure. S Afr J Sci 88:563–573

Renne PR, Deino AL, Walter RC, Turrin BD, Swisher CC III, Becker TA, Curtis GH, Sharp WD, Jaouni A-R (1994) Intercalibration of astronomical and radioisotopic time. Geology 22:783–786

Renne PR, Swisher CC III, Deino AL, Karner DB, Owens T, DePaolo DJ (1998) Intercalibration of standards, absolute ages and uncertainties in ^{40}Ar/^{39}Ar dating. Chem Geol 145:117–152

Rex DC, Guise PG (1986) Age of the Tinto Felsite, Lanarkshire; a possible 39/40 Ar monitor. Bull Liaison and Informations, IGCP Proj 196. Calibration Phanerozoic Time Scale 6:8–10

Samson SD, Alexander EC Jr (1987) Calibration of the interlaboratory ^{40}Ar/^{39}Ar dating standard, Mmhb-1. In: New developments and applications in isotope geoscience. Chem Geol (Isot Geosci Sect) 66:27–34

Schmid SM, Aebli HR, Heller F, Zingg A (1989) The role of the Periadriatic Line in the tectonic evolution of the Alps. In: Coward MP, Dietrich D, Park RG (eds) Alpine tectonics. Geol Soc Spec Publ 45:153–171

Seward D, Sibson RH (1985) Fission-track age for a pseudotachylite from the Alpine Fault zone, New Zealand. N Z J Geol Geophys 28:553–557

Sherlock SC, Hetzel R (2001) A laser-probe ^{40}Ar/^{39}Ar study of pseudotachylite from the Tambach Fault Zone, Kenya: direct isotopic dating of brittle faults. J Struct Geol 23:33–44

Sibson RH (1975) Generation of pseudotachylyte by ancient seismic faulting. Geophys J R Astron Soc 43:775–794

Spiess R (1995) The Passeier-Jaufen Line: a tectonic boundary between Variscan and Eo-Alpine Meran-Mauls basement. Schweiz Mineral Petrogr Mitt 75:413–425

Spray JG (1992) A physical basis for the frictional melting of some rock-forming minerals. In: Magloughlin JF, Spray JG (eds) Frictional melting processes and products in geological materials. Tectonophysics 204:205–221

Spray JG (1995) Pseudotachylyte controversy: Fact or friction? Geology 23:1119–1122

Spray JG, Kelley SP, Reimold WU (1995) Laser-probe argon-40/argon-39 dating of coesite- and stishovite-bearing pseudotachylytes and the age of the Vredefort impact event. Meteoritics 30:335–343

Steiger RH, Jäger E (1977) Subcommission on geochronology: convention on the use of decay constants in geo- and cosmochronology. Earth Planet Sci Lett 36:359–362

Thöni M (1981) Degree and evolution of the Alpine metamorphism in the Austroalpine Unit W of the Hohe Tauern in the light of K/Ar and Rb/Sr age determinations on micas. Jahrb Geol Bundesanstalt Wien 124:111–174

Thöni M (1988) Rb-Sr isotopic resetting in mylonites and pseudotachylites: implications for the detachment and thrusting of the Austroalpine basement nappes in the Eastern Alps. Jahrb Geol Bundesanstalt Wien 131:169–201

Trieloff M, Reimold WU, Kunz J, Boer RH, Jessberger EK (1994) ^{40}Ar-^{39}Ar thermochronology of pseudotachylite at the Ventersdorp Contact Reef, Witwatersrand basin. S Afr J Geol 97:365–384

Van der Pluijm BA, Hall CM, Vrolijk PJ, Pevear DR, Covey MC (2001) The dating of shallow faults in the Earth's crust. Nature 412:172–175

Villa IM (1991) Excess Ar geochemistry in potassic volcanites. Schweiz Mineral Petrogr Mitt 71:211–225

Villa IM (1997) Direct determination of ^{39}Ar recoil distance. Geochim Cosmochim Acta 61:689–691

Villa IM (2001) Radiogenic isotopes in fluid inclusions. Lithos 55:115–124

Villa IM, Ruggieri G, Puxeddu M (1997) Petrological and geochronological discrimination of two white- mica generations in a granite cored from the Larderello-Travale geothermal field (Italy). Eur J Mineral 9:563–568

Villa IM, Hermann J, Müntener O, Trommsdorff V (2000) ^{39}Ar-^{40}Ar dating of multiply zoned amphibole generations (Malenco, Italian Alps). Contrib Mineral Petrol 140:363–381

Viola G (2000) Kinematics and timing of the Periadriatic fault system in the Giudicarie region (central-eastern Alps). PhD Thesis, ETH Zürich no 13590, p 205

Von Blanckenburg F, Villa IM, Baur H, Morteani G, Steiger RH (1989) Time calibration of a PT-path from the Western Tauern Window, Eastern Alps: the problem of closure temperatures. Contrib Mineral Petrol 101:1–11

Wagreich M, Faupl P (1994) Paleogeography and geodynamic evolution of the Gosau Group of the Northern Calcareous Alps (Late Cretaceous, Eastern Alps, Austria). Palaeogeogr Palaeoclimat Palaeoecol 110:235–254

Werling E (1992) Tonale-, Pejo- und Judicarien-Linie: Kinematik, Mikrostrukturen und Metamorphose von Tektoniten aus räumlich interferierenden aber verschiedenaltrigen Verwerfungszonen. PhD Thesis, ETH Zürich no 9923, p 270

White JC (1993) Shock-induced melting and silica polymorph formation, Vredefort Structure, South Africa. In: Boland JN, FitzGerald JD (eds) Defects and processes in the solid state: geoscience applications (The McLaren Volume). Elsevier, Amsterdam, pp 69–84